The Dramatic Size and Kinematic Evolution of Massive Early-type Galaxies

A. Lapi[1,2,3] , L. Pantoni[1,4], L. Zanisi[5], J. Shi[6], C. Mancuso[4], M. Massardi[4], F. Shankar[5] , A. Bressan[1,3] , and L. Danese[1,2,3]

[1] SISSA, Via Bonomea 265, I-34136 Trieste, Italy
[2] INFN-Sezione di Trieste, via Valerio 2, I-34127 Trieste, Italy
[3] INAF-Osservatorio Astronomico di Trieste, via Tiepolo 11, I-34131 Trieste, Italy
[4] INAF-IRA, Via P. Gobetti 101, I-40129 Bologna, Italy
[5] Dept. of Physics and Astronomy, University of Southampton, Southampton SO17 1BJ, UK
[6] Dept. of Astronomy, Univ. of Science and Technology of China, Hefei, 230026 Anhui, People's Republic of China

Abstract

We aim to provide a holistic view on the typical size and kinematic evolution of massive early-type galaxies (ETGs) that encompasses their high-z star-forming progenitors, their high-z quiescent counterparts, and their configurations in the local Universe. Our investigation covers the main processes playing a relevant role in the cosmic evolution of ETGs. Specifically, their early fast evolution comprises biased collapse of the low angular momentum gaseous baryons located in the inner regions of the host dark matter halo; cooling, fragmentation, and infall of the gas down to the radius set by the centrifugal barrier; further rapid compaction via clump/gas migration toward the galaxy center, where strong heavily dust-enshrouded star formation takes place and most of the stellar mass is accumulated; and ejection of substantial gas amount from the inner regions by feedback processes, which causes a dramatic puffing-up of the stellar component. In the late slow evolution, passive aging of stellar populations and mass additions by dry merger events occur. We describe these processes relying on prescriptions inspired by basic physical arguments and by numerical simulations to derive new analytical estimates of the relevant sizes, timescales, and kinematic properties for individual galaxies along their evolution. Then we obtain quantitative results as a function of galaxy mass and redshift, and compare them to recent observational constraints on half-light size R_e, on the ratio v/σ between rotation velocity and velocity dispersion (for gas and stars) and on the specific angular momentum $j_\star$ of the stellar component; we find good consistency with the available multiband data in average values and dispersion, both for local ETGs and for their $z \sim 1$–2 star-forming and quiescent progenitors. The outcomes of our analysis can provide hints to gauge sub-grid recipes implemented in simulations, to tune numerical experiments focused on specific processes, and to plan future multiband, high-resolution observations on high-redshift star-forming and quiescent galaxies with next-generation facilities.

Key words: galaxies: evolution – galaxies: fundamental parameters – galaxies: high-redshift – galaxies: kinematics and dynamics – galaxies: structure

1. Introduction

The formation and evolution of massive early-type galaxies (ETGs) has been one of the hottest and most debated issue in the astrophysics research of the last decades.

It has been established a long time ago that ETGs endowed with stellar masses $M_\star \gtrsim 3 \times 10^{10} M_\odot$ feature homogeneous stellar populations with average ages $\gtrsim 7$–10 Gyr, pointing toward a typical formation redshift $z \gtrsim 1$ (e.g., Renzini 2006 and references therein). The associated star formation efficiency $f_\star \equiv M_\star/f_b M_H$, i.e., the ratio between the stellar mass to that $f_b M_H \approx 0.16 M_H$ of the baryons originally present in the host dark matter (DM) halo, is found to be substantially below unity, with values $f_\star \lesssim 0.2$ consistently inferred from weak-lensing observations (Velander et al. 2014; Hudson et al. 2015; Mandelbaum et al. 2016) and abundance matching arguments (e.g., Shankar et al. 2006; Aversa et al. 2015; Rodriguez-Puebla et al. 2015; Moster et al. 2017); on the other hand, these systems are characterized by a high stellar metallicity $Z_\star \gtrsim Z_\odot$, with values around or even exceeding the solar one (e.g., Thomas et al. 2005; Gallazzi et al. 2014). This suggests that most of the stellar mass must be accumulated in a very intense star formation episode, and that after quenching, further gas must be hindered from infall because of heating/ejection to avoid substantial metal dilution.

This picture is reinforced by the pronounced α–enhancement observed in massive ETGs; this has to be interpreted as an iron underabundance compared to α elements, caused by the quenching of the star formation before Type Ia supernova explosions can pollute the interstellar medium with substantial iron amounts (e.g., Thomas et al. 2005; Gallazzi et al. 2006, 2014). The implied star formation timescales, somewhat dependent on the assumed initial mass function (IMF), boil down to a fraction of Gyr. As to the mechanism responsible for the quenching, the most likely possibility involves energy feedback from the central supermassive black hole (BH). Indeed, relic BHs are known to be hosted at the center of almost all massive ETGs, with masses $M_{BH} \sim 10^7$–$10^{10} M_\odot$ that correlate strongly with many galaxy properties (e.g., with the stellar mass in the old stellar population, with the Sérsic index of the light profile, and most fundamentally with the stellar velocity dispersion), suggesting a coevolution in the build-up of the BH and of the stellar component (see Kormendy & Ho 2013 and references therein; Shankar et al. 2016; van den Bosch 2016).

Two relatively recent findings have shed further insight on the processes at work in the formation of massive ETGs. The first piece of news concerns the identification via deep near-IR surveys of an increasing number of quiescent massive galaxies at high redshifts $z \gtrsim 2$ (see Cimatti et al. 2004; Ilbert et al. 2013; Duncan et al. 2014; Tomczak et al. 2014; Caputi et al. 2015;

Grazian et al. 2015; Song et al. 2016; Davidzon et al. 2017; Glazebrook et al. 2017), which are found to be already in passive evolution and to feature chemical properties similar to local ETGs (e.g., Cimatti et al. 2008; van Dokkum et al. 2008), including (super-) solar metallicity and a pronounced α-enhancement.

The second piece of news concerns the discovery of an abundant population of dusty star-forming galaxies at redshifts $z \gtrsim 1$, which has been shown to be responsible for the bulk of the cosmic star formation history out to $z \lesssim 4$ (e.g., Lapi et al. 2011, 2017b; Gruppioni et al. 2013, 2015; Rowan-Robinson et al. 2016; Bourne et al. 2017; Dunlop et al. 2017; Novak et al. 2017), and to contribute even at $z \sim 6$ (e.g., Cooray et al. 2014; Riechers et al. 2017; Schreiber et al. 2018; Strandet et al. 2017; Zavala et al. 2018). This achievement has become feasible thanks to wide-area far-IR/submillimeter surveys (e.g., Lapi et al. 2011; Gruppioni et al. 2013, 2015; Weiss et al. 2013; Koprowski et al. 2014, 2016; Strandet et al. 2016), in many instances facilitated by gravitational lensing from foreground objects (e.g., Negrello et al. 2014, 2017; Nayyeri et al. 2016). In fact, galaxies endowed with star formation rates (SFRs) exceeding some tens $M_\odot \, \mathrm{yr}^{-1}$ at redshift $z \gtrsim 2$ were largely missed by rest-frame optical/UV surveys because of heavy dust obscuration, which is difficult to correct for with standard techniques based only on UV spectral data (e.g., Bouwens et al. 2016, 2017; Mancuso et al. 2016a; Ikarashi et al. 2017; Pope et al. 2017; Simpson et al. 2017).

Follow-up optical and near-/mid-IR observations of these dusty star-forming galaxies have allowed their stellar mass content to be characterized. The vast majority features stellar masses strongly correlated with the SFR, in the way of an almost linear relationship (the so-called "main sequence") with a limited scatter around 0.25 dex (see Rodighiero et al. 2011, 2015; Speagle et al. 2014; Salmon et al. 2015; Tasca et al. 2015; Kurczynski et al. 2016; Tomczak et al. 2016; Santini et al. 2017; Schreiber et al. 2017). In addition, huge molecular gas reservoirs are found in these star-forming systems (Scoville et al. 2014, 2016, 2017; Béthermin et al. 2015; Aravena et al. 2016; Decarli et al. 2016; Huynh et al. 2017; Jimenez-Andrade et al. 2018), in many instances consistent with the local, integrated Schmidt–Kennicutt diagram (SFR versus mass of molecular gas).

X-ray follow-up observations of dusty star-forming galaxies have revealed the growth of the central supermassive BH before it attains a high enough mass and power to manifest as a quasar, to quench star formation, and to evacuate gas and dust from the host (e.g., Alexander & Hickox 2012 and references therein; Mullaney et al. 2012; Page et al. 2012; Johnson et al. 2013; Delvecchio et al. 2015; Rodighiero et al. 2015; Stanley et al. 2015, 2017); intriguing correlations between the nuclear power and the host stellar mass and SFR have been established. Recently, even earlier stages in the growth of the BH have been revealed by targeted X-ray observations in a gravitationally lensed, far-IR selected galaxy at $z \sim 2$ (Massardi et al. 2018).

These findings consistently support an in situ coevolution scenario for star formation and BH accretion, envisaging these as local, time-coordinated, and interlinked processes (e.g., Lapi et al. 2011, 2014, 2017a). This view is corroborated by recent studies based on the continuity equation for the stellar component of galaxies; in a closely model-independent way, these have demonstrated that dusty star-forming galaxies constitute the progenitors of high-z massive quiescent galaxies

and eventually, of local massive ETGs (Mancuso et al. 2016a, 2016b; Lapi et al. 2017a).

Here we focus on two other important aspects of ETGs and of their quiescent and star-forming progenitors that can offer additional clues on galaxy formation and evolution. One is related to the size of these systems, typically measured in terms of major axis (or circularized) half-light radius R_e. The other concerns kinematical properties, and specifically, the ratio v/σ of rotation velocity to velocity dispersion.

Local massive ETGs follow a rather tight direct relationship between half-light size R_e and stellar mass $M_\star$ (see Shen et al. 2003; Cappellari et al. 2013; Cappellari 2016). Their stellar kinematics is largely dominated by random motions, with velocity ratio $(v/\sigma)_\star \lesssim 1$ (see Cappellari et al. 2013); in particular, most ETGs are regular rotators with $(v/\sigma)_\star \sim 0.2$–1, while a small fraction of slow rotators features values $(v/\sigma)_\star \lesssim 0.2$. We note that from theoretical arguments, the $(v/\sigma)_\star$ ratio is expected to depend on the intrinsic ellipticity (e.g., Binney 2005; Emsellem et al. 2007; Cappellari 2016), but marginalizing over this quantity yields a definite, if somewhat dispersed, relationship with stellar mass (Veale et al. 2017).

Massive quiescent progenitors of ETGs at high redshift are known to be significantly more compact, by factors 3–5, than local ETGs at given stellar mass (Daddi et al. 2005; Trujillo et al. 2006; Cimatti et al. 2008; van Dokkum et al. 2008; van de Sande et al. 2013; Belli et al. 2014, 2017; van der Wel et al. 2014; Straatman et al. 2015). On the other hand, kinematical studies are difficult and scarce at $z \gtrsim 1$; the sample around $z \sim 1$ by van der Wel & van der Marel (2008) appears to indicate an appreciably higher $(v/\sigma)_\star$ ratio than in local ETGs, and the trend is confirmed by the kinematical analysis of a $z \sim 2$ gravitationally lensed galaxy (Newman et al. 2015).

As to star-forming ETG progenitors, early observations in the near-IR/optical bands indicated quite large sizes, comparable to or even exceeding those of high-redshift quiescent galaxies (e.g., van Dokkum et al. 2014; Shibuya et al. 2015). However, more recent high-resolution observations in the far-IR/(sub-)millimeter/radio band via ground-based interferometers (including ALMA) have revealed dusty star formation to occur in a few collapsing clumps distributed over scales $\lesssim 2 \, \mathrm{kpc}$, substantially smaller than for quiescent galaxies with similar stellar mass (see Barro et al. 2014, 2016b; Ikarashi et al. 2015; Simpson et al. 2015; Straatman et al. 2015; Hodge et al. 2016; Spilker et al. 2016; Tadaki et al. 2017a, 2017b; Massardi et al. 2018; see also Almaini et al. 2017). Kinematical studies reveal the presence of a strongly baryon-dominated stellar core with high ongoing dusty SFR $\gtrsim$ some $10^2 \, M_\odot \, \mathrm{yr}^{-1}$, surrounded out to ~ 15–20 kpc by a clumpy, unstable gaseous disk in nearly Keplerian rotation (Genzel et al. 2014, 2017; van Dokkum et al. 2015; Wisnioski et al. 2015; Burkert et al. 2016; Swinbank et al. 2017; Tadaki et al. 2017a, 2017b; Talia et al. 2018); this corresponds to a high ratio $v/\sigma \gtrsim 3$ for the gas component, mainly determined by a substantial rotation velocity $v \gtrsim 250 \, \mathrm{km \, s}^{-1}$ and by a modest intrinsic velocity dispersion $\sigma \lesssim 30$–80 km s^{-1} related to turbulent motions (see Law et al. 2009; Genzel et al. 2011; Wisnioski et al. 2015; Turner et al. 2017; Johnson et al. 2018).

A variety of processes has been invoked in the literature to explain such a complex observational landscape. For example, the early growth of a gaseous clumpy disk in high-redshift galaxies may be fed by cold gas streams from large-scale filaments of the cosmic web (e.g., Birnboim & Dekel 2003; Dekel et al. 2009) or by a biased collapse of the baryons in the

inner region of the halo (e.g., Lapi et al. 2011, 2014, 2017a; Romanowsky & Fall 2012; Lilly et al. 2013; Shi et al. 2017); the subsequent compaction may be triggered by violent disk instabilities (e.g., Dekel & Burkert 2014; Bournaud 2016) or by wet mergers (e.g., Mihos & Hernquist 1996; Hopkins et al. 2006); the quenching of the star formation and puffing-up into more extended configurations may involve energy/momentum feedback from supernovae and stellar winds (e.g., White & Frenk 1991; Cole et al. 2000; Murray et al. 2005) and from the central supermassive BH during its quasar phase (e.g., Silk & Rees 1998; Granato et al. 2004; Fan et al. 2008, 2010; Lapi et al. 2014), or gravitational quenching (e.g., Dekel & Birnboim 2008; Khochfar & Ostriker 2008); finally, the late growth in size of a quiescent galaxy is thought to originate via dry merger events (e.g., Khochfar & Silk 2006; Ciotti & Ostriker 2007; Naab et al. 2009). We further stress that when considering the data ensemble for both high-z star-forming and quiescent galaxies, a critical observational finding is that the measured sizes are significantly more scattered than for local ETGs (see Fan et al. 2008, 2010), although part of this effect can be ascribed to an observational bias for star-forming systems. Therefore a major theoretical challenge is to identify a fundamental mechanism along the ETG evolution that must account for an appreciable reduction in the size spread.

In this paper we aim to provide a physical description of the main processes responsible for the typical size and kinematics evolution of massive ETGs, including their high-redshift star-forming progenitors, their high-redshift quiescent counterparts, and their final configurations in the local Universe. Our methods are mainly (semi-)analytic, but are heavily based on detailed outcomes from state-of-the-art numerical experiments and simulations on specific processes, such as puffing-up by stellar/BH feedback and dry merging. The quantitative results of our analysis are compared in terms of average values and dispersions with the most recent observational constraints on galaxy sizes and kinematics at different redshifts, which provides indications for tuning numerical experiments that are focused on specific processes.

The plan of the paper is as follows: in Section 2 we recall the basic notions of the biased collapse scenario for ETG formation. In Section 3 we discuss the theoretical aspects of the size and kinematics evolution of ETG progenitors, which includes gas cooling, infall, and fragmentation (Section 3.1), clump migration and compaction (Section 3.2), puffing-up by feedback processes (Section 3.3), and late-time evolution by dry mergers (Section 3.4). Quantitative results and their comparison with observations are presented in Section 4, and finally, our findings are discussed and summarized in Section 5.

Throughout this work, we adopt the standard flat cosmology (Planck Collaboration XIII 2016) with rounded parameter values: matter density $\Omega_M = 0.32$, baryon density $\Omega_b = 0.05$, Hubble constant $H_0 = 100\,h\ \mathrm{km\ s^{-1}\ Mpc^{-1}}$ with $h = 0.67$, and mass variance $\sigma_8 = 0.83$ on a scale of $8\,h^{-1}$ Mpc. Reported stellar masses and SFRs (or luminosities) of galaxies refer to the Chabrier (2003) IMF.

2. Biased Collapse of ETG Progenitors

In this section we focus on basic aspects of the biased collapse scenario for the formation of ETG progenitors (see Eke et al. 2000; Fall 2002; Romanowsky & Fall 2012; Shi et al. 2017) that is then exploited to investigate their early evolution.

Given a halo of mass M_H, we define its virial radius as $R_H \equiv [3\,M_H/4\pi\,\rho_c\,\Delta_H\,E_z]^{1/3}$, where $\rho_c \approx 2.8 \times 10^{11}\,h^2\,M_\odot\ \mathrm{Mpc}^{-3}$ is the critical density, $\Delta_H \simeq 18\,\pi^2 + 82\,[\Omega_M(1+z)^3/E_z - 1] - 39\,[\Omega_M(1+z)^3/E_z - 1]^2$ is the nonlinear density contrast at collapse, and $E_z = \Omega_\Lambda + \Omega_M(1+z)^3$ is a redshift-dependent factor. In the following we conveniently express the virial radius R_H and circular velocity $v_{c,H}^2 \equiv GM_H/R_H$ of the halo in terms of the stellar mass $M_\star$ enclosed in the host galaxy and of its star formation efficiency $f_\star \equiv M_\star/f_b M_H$, where $f_b \equiv \Omega_b/\Omega_M \approx 0.16$ is the universal baryon to DM mass ratio. The outcome reads

$$R_H \approx 160\,f_{\star,0.2}^{-1/3}\,M_{\star,11}^{1/3}\,[E_z/E_{z=2}]^{-1/3}\ \mathrm{kpc},$$
$$v_{c,H} \approx 300\,f_{\star,0.2}^{-1/3}\,M_{\star,11}^{1/3}\,[E_z/E_{z=2}]^{1/6}\ \mathrm{km\ s^{-1}}, \qquad (1)$$

where we have introduced the normalized quantities $M_{\star,11} = M_\star/10^{11}\,M_\odot$, $f_{\star,0.2} \equiv f_\star/0.2$, and we have chosen $z \approx 2$ as the fiducial formation redshift of ETG progenitors (see discussion below). The related dynamical time is

$$t_{\mathrm{dyn}}(R_H) \simeq \frac{\pi}{2}\sqrt{\frac{R_H^3}{G\,M_H}} \approx 8.5 \times 10^8\,[E_z/E_{z=2}]^{-1/2}\ \mathrm{years}. \qquad (2)$$
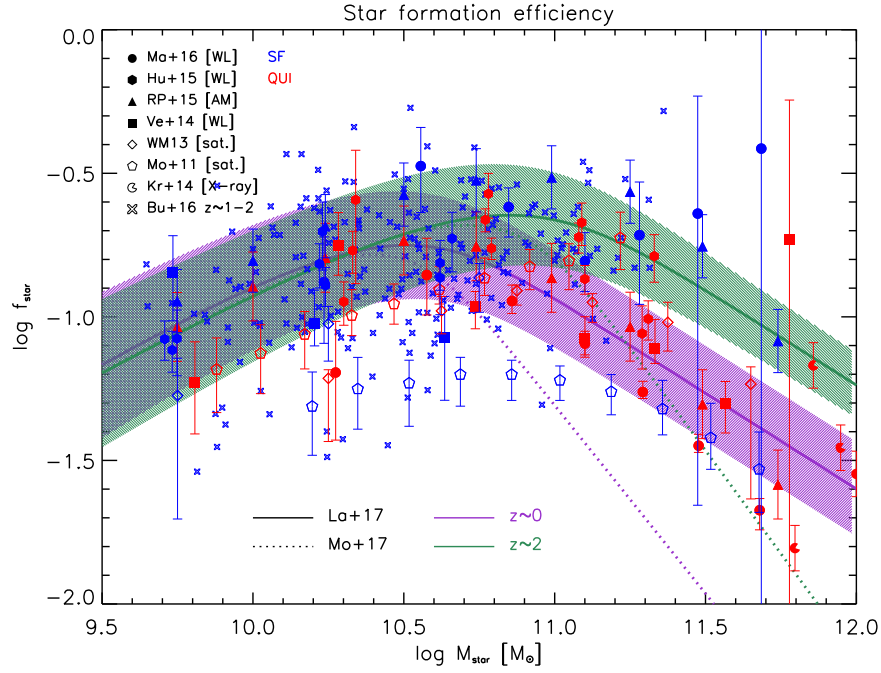
The star formation efficiency $f_\star$ as a function of stellar mass $M_\star$ for central galaxies has been estimated at different redshifts based on abundance matching techniques (see Behroozi et al. 2013; Moster et al. 2013, 2017; Aversa et al. 2015; Rodriguez-Puebla et al. 2015; Shi et al. 2017), and has been checked against local observations from weak lensing (e.g., Velander et al. 2014; Hudson et al. 2015; Mandelbaum et al. 2016), satellite kinematics (e.g., More et al. 2011; Wojtak & Mamon 2013), X-ray halos around bright cluster galaxies (BCGs; Gonzalez et al. 2013; Kravtsov et al. 2014), and recently against estimates at $z \sim 1$–2 from mass profile modeling (see Burkert et al. 2016).

The outcomes at $z \approx 0$ (magenta solid line) and 2 (green solid line) obtained by Lapi et al. (2017a) from abundance matching of the galactic halo mass function and of the stellar mass function from the continuity equation are illustrated in Figure 1. For comparison, the results from an empirical model of galaxy formation by Moster et al. (2017) are also shown. The efficiency is a nonmonotonic function of the stellar mass with maximal values $f_\star \approx 0.15$–0.25 around $M_\star \approx 10^{10}$ to a few $10^{11}\,M_\odot$, decreasing to less than 5% for $M_\star \lesssim$ a few $10^9\,M_\odot$ and for $M_\star \gtrsim$ a few $10^{11}\,M_\odot$.

From the above quantities, the specific (i.e., per unit mass) angular momentum j_H of the halo is usually specified in terms of the dimensionless spin parameter λ as

$$j_H \equiv \sqrt{2}\,\lambda\,R_H\,v_{c,H} \approx 2.4 \times 10^3\,\lambda_{0.035}\,f_{\star,0.2}^{-2/3}\,M_{\star,11}^{2/3}$$
$$\times\,[E_z/E_{z=2}]^{-1/6}\ \mathrm{km\ s^{-1}\,kpc}, \qquad (3)$$

where $\lambda_{0.035} \equiv \lambda/0.035$. Numerical simulations (see Barnes & Efstathiou 1987; Bullock et al. 2001; Macciò et al. 2007; Zjupa & Springel 2017) have shown that λ exhibits a log-normal distribution with average value $\langle\lambda\rangle \approx 0.035$ and dispersion $\sigma_{\log\lambda} \approx 0.25$ dex, nearly independent of mass and redshift. Moreover, the halo-specific angular momentum is found to follow a radial distribution $j_H(<r) \propto M_H(<r)^s$ with slope $s \approx 1$, also nearly independent of mass and redshift (e.g., Bullock et al. 2001; Shi et al. 2017).

Figure 1. Star formation efficiency $f_{\rm star} \equiv M_\star/f_b\,M_{\rm H}$ vs. stellar mass $M_\star$. Solid lines with shaded areas illustrate the outcome by Lapi et al. (2017a) via abundance matching of the halo and stellar mass functions at $z \approx 0$ (green) and $z \approx 2$ (magenta); for reference, the dotted lines refer to the results from the empirical model by Moster et al. (2017). Data points (red for quiescent and blue for star-forming galaxies) are from Mandelbaum et al. (2016; circles), Hudson et al. (2015; hexagons) and Velander et al. (2014; squares) via weak lensing, Rodriguez-Puebla et al. (2015; triangles) via subhalo abundance matching, Wojtak & Mamon (2013; diamonds) and More et al. (2011; pentagons) via satellite kinematics, Kravtsov et al. (2014, pacmans) via X-ray observations of BCGs, and Burkert et al. (2016; crosses) via mass profile modeling at $z \sim 1$–2.

The classic assumption envisages that the mass distribution of the baryons and the DM mirror each other initially; this implies that $j_b(<r) = j_{\rm H}(<r)$. However, the biased collapse scenario (see Eke et al. 2000; Fall 2002; Romanowsky & Fall 2012; Shi et al. 2017) envisages that only a fraction $f_{\rm inf} = M_{\rm inf}/f_b\,M_{\rm H}$ of the available baryons within the halo is able to cool and fall in toward the central region of the galaxy where star formation takes place; under such circumstances, the specific angular momentum $j_{\rm inf}$ associated with the infalling baryons is expected to be somewhat lower than $j_{\rm H}$. In fact, one can write

$$j_{\rm inf} = f^s_{\rm inf}\,j_{\rm H} \approx 1.4 \times 10^3\,\lambda_{0.035}\,f^s_{\rm inf,0.6}\,f^{-2/3}_{\star,0.2}\,M^{2/3}_{\star,11}$$
$$\times\,[E_z/E_{z=2}]^{-1/6}\,{\rm km\ s}^{-1}\,{\rm kpc}, \qquad (4)$$

with the normalization $f_{\rm inf,0.6} \equiv f_{\rm inf}/0.6$ discussed below. Finally, the specific angular momentum $j_\star$ retained/sampled in the local Universe by the stellar component is a fraction of $j_{\rm inf}$.

Shi et al. (2017) have been the first to infer the infall fraction $f_{\rm inf}$ in ETGs by exploiting diverse observations on the star formation efficiency and the chemical abundance. Based on simple mass and metal conservation arguments, these authors found that the infall fraction can be closely estimated as

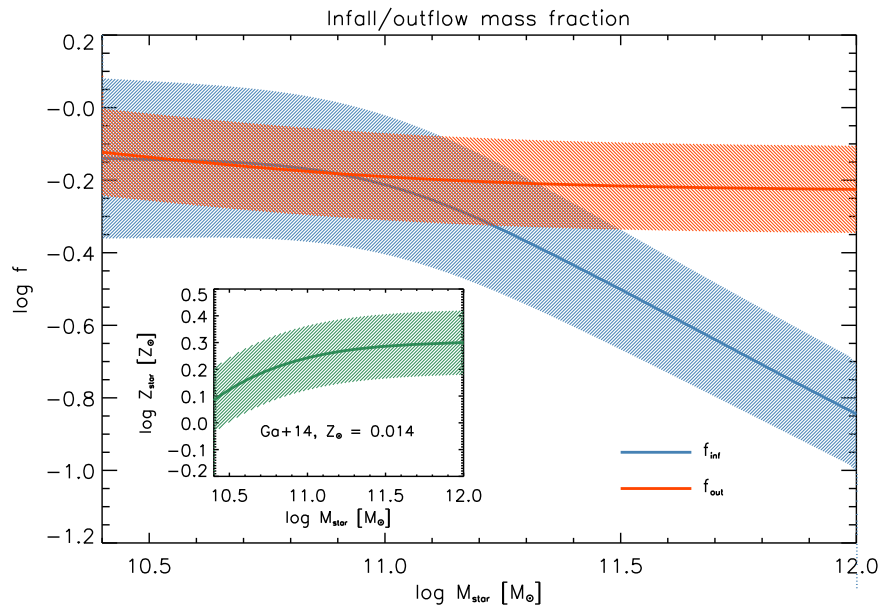$$f_{\rm inf} \simeq \frac{y_Z\,f_\star}{Z_\star}, \qquad (5)$$

in terms of the effective true metal yield of a single stellar population y_Z, of the star formation efficiency $f_\star$, and of the stellar metallicity $Z_\star$. This approximated estimate for ETGs provides outcomes to within 10% accuracy relative to the exact expression derived by Shi et al. (2017; see their Section 3 and in particular Equations (11)–(13)). However, the various quantities entering Equation (5) are subject to observational and systematic uncertainties that we now briefly discuss in turn.

For the star formation efficiency $f_\star$ at $z \approx 2$, we adopt the dependence on $M_\star$ and the associated scatter from Figure 1. Note that the determination of the efficiency at high stellar masses $M_\star \gtrsim 10^{12}\,M_\odot$ is rather uncertain because of difficulties in accounting for faint stellar outskirts; however, the effect should be less relevant at high redshift $z \sim 2$, since outer stellar masses are thought to be accumulated at late cosmic times $z \lesssim 1$ via dry mergers (e.g., Rodriguez-Gomez et al. 2015, 2016; Buitrago et al. 2017).

For the average metal yield, we adopt the fiducial value $y_Z \approx 0.069$ appropriate for a Chabrier IMF, solar metallicity, and the Romano et al. (2010) stellar yield models (see also Krumholz & Dekel 2012; Feldmann 2015; Vincenzo et al. 2016). We also allow for a systematic dispersion within the range $y_Z \sim 0.05$–0.08 that embraces values for different chemical compositions and stellar yield models (e.g., Romano et al. 2010; Nomoto et al. 2013; Vincenzo et al. 2016). It is worth noting that for a massive galaxy formed at $z \approx 2$ with a star formation duration of $\lesssim 1$ Gyr, the metal yield y_Z changes by less than 30% from the epoch of quenching to the present time.

For the stellar metallicity for ETGs, we adopt the average determination $Z_\star(M_\star)$ as a function of stellar mass at $z \approx 0$ and the associated scatter around 0.15 dex by Gallazzi et al. (2014). There is clear evidence both from local massive ETGs (e.g., Gallazzi et al. 2006, 2014; Choi et al. 2014; Citro et al. 2016; Siudek et al. 2017) and from their quiescent high-redshift counterparts (e.g., Lonoce et al. 2015; Kriek et al. 2016) that after the main burst of star formation, the metal abundance in the bulk of the stellar component stays approximately constant. Although late-time accretion of stripped stars via minor dry

Figure 2. Fractions of infalling f_{inf} and outflowing f_{out} mass vs. stellar mass $M_\star$. The solid lines illustrate the average infall mass fraction $f_{inf} \simeq y_Z f_{star}/Z_\star$ (blue) and outflow mass fraction $f_{out} \simeq 1 - Z_\star/y_Z$ (orange); the shaded areas show the corresponding scatter. In the inset the solid green line illustrates the adopted average stellar metallicity $Z_\star$ vs. stellar mass $M_\star$ relationship from Gallazzi et al. (2014) for local ETGs, renormalized for a solar metallicity $Z_\odot \approx 0.014$, and the shaded area shows the associated scatter.

mergers (e.g., Rodriguez-Gomez et al. 2016; Buitrago et al. 2017) may contribute to flattening the metal gradient toward the outermost regions of local ETGs, the net effect on the average metallicity is mild (e.g., Yildirim et al. 2017; Martin-Navarro et al. 2018). Therefore, we reasonably assume that the average metallicity of present-day massive ETGs was already in place at redshift $z \sim 2$. It is also worth noting that the determination by Gallazzi et al. (2014) is based on a combination of stellar absorption indices that constitutes an unbiased diagnostic tool for the simultaneous derivation of ages, metallicities, and α/Fe ratios; this dispenses with, or at least strongly alleviates, the systematic uncertainties related to measurements of metallicity from Fe abundances and hence on the occurrence rate of supernova Type Ia per unit SFR (e.g., Annibali et al. 2007).

The resulting dependence of the infall fraction f_{inf} on the stellar mass at $z \approx 2$ is illustrated in Figure 2 (the stellar metallicity is plotted in the inset); it features typical values ranging from $f_{inf} \approx 0.7$ to 0.6 to 0.2 for $M_\star$ increasing from a few 10^{10} to 10^{11} to $10^{12} M_\odot$, and logarithmic scatter around $\sigma_{\log f_{inf}} \approx 0.25$ dex. This behavior is indeed consistent with a scenario of biased collapse where only a fraction of the gas initially present in the halo is processed within the central regions.

Exploiting this determination of f_{inf}, Shi et al. (2017; cf. their Figure 5(a)) have compared the predicted j_{inf} from Equation (4) against the locally observed $j_\star$ versus $M_\star$ relationship for ETGs, finding a good agreement and explaining its parallel shape and lower normalization with respect to that of local spiral galaxies. Moreover, by comparing with kinematics observations (van Dokkum et al. 2015; Barro et al. 2017; Tadaki et al. 2017a) of massive galaxies at $z \sim 2$, Shi et al. (2017 cf. their Figure 5(b)) also confirmed an additional prediction of the biased collapse scenario, i.e., that the specific angular momentum of ETG progenitors at $z \sim 2$ is imprinted since their formation (when $\gtrsim 70\%$ of their mass gets in place), with minor changes due to

dry merging at late cosmic times (e.g., Rodriguez-Gomez et al. 2015, 2016; Buitrago et al. 2017). In conclusion, the biased collapse scenario and the associated values of f_{inf} are quantitatively corroborated by these two independent sets of observations.

3. Size and Kinematics of ETG Progenitors

In this section we focus on the main processes at work in determining the size and kinematic evolution of ETG progenitors. These are schematically depicted in the cartoon of Figure 3 and comprise biased collapse of the low angular momentum gaseous baryons located in the inner regions of the host DM halo; cooling, fragmentation, and infall of the gas down to the radius set by the centrifugal barrier; further rapid compaction via clump/gas migration toward the galaxy center, where strong and heavily dust-enshrouded star formation activity takes place and most of the stellar mass is accumulated; ejection of substantial amount of gas from the inner regions by feedback processes and dramatic puffing-up of the stellar component; and passive aging of stellar populations and mass additions by dry merger events. We now describe each of these processes with prescriptions inspired by basic physical arguments and by numerical simulations, and derive new analytical estimates of the relevant sizes, timescales, and kinematic properties for individual galaxies throughout their evolution. In the scaling relations of this section, we normalize the star formation efficiency $f_\star \approx 0.2$ and the infall fraction $f_{inf} \approx 0.6$ to the values applying for a reference mass $M_\star \approx 10^{11} M_\odot$ for clarity. In Section 4 we exploit the full mass dependence and dispersion of these quantities to quantitatively compare our results with the available observations.

3.1. Cooling and Fragmentation

We start by computing the initial radius R_{inf} that encloses the infalling mass $M_{inf} = f_{inf} f_b M_H$ subject to the biased collapse (see Section 2). For the radial range of interest, we can assume

that the baryon and DM mass approximately scale with radius as[7] $M(<r) \propto r$, so that

$$R_{\rm inf} \approx f_{\rm inf} \, R_{\rm H} \approx 96 \, f_{\rm inf,0.6} \, f_{\star,0.2}^{-1/3} \, M_{\star,11}^{1/3} \, [E_z/E_{z=2}]^{-1/3} \ {\rm kpc}. \tag{6}$$

Note that the size $R_{\rm inf}$ is consistent with the scale over which observations (see Hodge et al. 2013; Karim et al. 2013; Simpson et al. 2015; Hill et al. 2017) and high-resolution simulations (see Narayanan et al. 2015) both indicate that gas, possibly segregated in multiple components, flows in toward the central regions of galaxy halos. The corresponding dynamical time reads

$$
\begin{aligned}
t_{\rm dyn}(R_{\rm inf}) &\simeq \frac{\pi}{2} \sqrt{\frac{R_{\rm inf}^3}{G \, M_{\rm H}(<R_{\rm inf})}} = f_{\rm inf} \, t_{\rm dyn}(R_H) \\
&\approx 5 \times 10^8 \, f_{\rm inf,0.6} \, [E_z/E_{z=2}]^{-1/2} \ {\rm years}.
\end{aligned} \tag{7}
$$

We emphasize that a high formation redshift $z \gtrsim 1.5$ and a low infall fraction $f_{\rm inf} \lesssim 0.6$ enforced by the biased collapse work together to set a rather short dynamical timescale that drives the subsequent evolution of ETG progenitors. For comparison, local spiral galaxies would feature a higher infall fraction $f_{\rm inf} \approx 1$ (see Shi et al. 2017) and a lower formation redshift $z \lesssim 1$, which would imply appreciably longer dynamical timescales of $\gtrsim$ a few Gyr.

On the other hand, the radiative cooling time writes (see Sutherland & Dopita 1993)

$$t_{\rm cool} \simeq \frac{2.5 \times 10^8}{\Lambda_{-23}(T, Z)} \frac{T_6}{n_{-3} \, \mathcal{C}_{10}} \ {\rm years}, \tag{8}$$

where $T_6 \equiv T/10^6 K$ is the temperature, $n_{-3} \equiv n/10^{-3} \ {\rm cm}^{-3}$ is the gas density, $\mathcal{C}_{10} \equiv \mathcal{C}/10$ is the clumping factor, and $\Lambda_{-23} \equiv \Lambda(T, Z)/10^{-23} \ {\rm cm}^3 \ {\rm s}^{-1} \ K$ is the cooling function in cgs units dependent on temperature and metallicity. The normalizations have been chosen to meet the values appropriate for ETG progenitors: the infalling gas is expected to have temperatures close to the virial $T_{\rm vir} \approx 3 \times 10^6 \, f_\star^{-2/3} \, M_{\star,11}^{2/3} \, [E_z/E_{z=2}]^{1/3} \ K$, and correspondingly $\Lambda_{-23} \gtrsim 1–2$ for $Z \gtrsim Z_\odot/10$; the gas density is expected to be on the order of the average baryon density within $R_{\rm inf}$, which reads $n \approx 2 \times 10^{-3} \, f_{\rm inf,0.6}^{-2} \, [E_z/E_{z=2}] \, (r/R_{\rm inf})^{-2} \ {\rm cm}^{-3}$; the clumping factor is expected to be higher than that of the IGM, which cosmological simulations (see Iliev et al. 2007; Pawlik et al. 2009; Finlator et al. 2012; Shull et al. 2012) indicate attains values $\mathcal{C} \sim 6–20$ at $z \approx 2$. From the above it is easily understood that the cooling time $t_{\rm cool}(r) \sim 4 \times 10^8 (r/R_{\rm inf})^{-2}$ years within $r \lesssim R_{\rm inf}$ is comparable to or shorter than the dynamical time, so that the gas can effectively cool and fall in over the timescale $t_{\rm dyn}(R_{\rm inf})$. We note that such gas is rotating, being endowed with the specific angular momentum $j_{\rm inf}$ given by Equation (4).

The fraction of gas that becomes available for star formation during the infall can be addressed by considering the fragmentation of the rotating material. Rotating disks are stable to gravitational fragmentation as far as the Toomre (1964) parameter $Q \equiv \sqrt{2} \, \Omega \, \sigma/\pi \, G\Sigma$ exceeds the critical values $0.7 - 1 - 2$ (for thick, thin, and composite disks, respectively), where $\Omega \equiv v/R \simeq j/R^2$ is the angular rotation velocity, σ is the intrinsic velocity dispersion of the gas, generally related to turbulent motions (note that the ISM is likely to become multiphase after infall, see Braun & Schmidt 2012), and $\Sigma \simeq M_{\rm gas}(<R)/\pi \, R^2$ is the gas surface density. The Toomre parameter can be arranged in terms of the gas mass contrast $\delta_{\rm gas}(R) \equiv M_{\rm gas}(<R)/M_{\rm tot}(<R)$, i.e., the ratio between the gas mass and the total mass (including DM), to simply read (see Dekel & Burkert 2014)

$$Q \approx \frac{\sqrt{2}}{\delta_{\rm gas}} \frac{\sigma}{v}. \tag{9}$$

The condition $Q \sim 1$ defines the stability radius $R_{\rm Q}$.

In absence of substantial fragmentation, the specific angular momentum $j_{\rm inf}$ is approximately conserved (e.g., Mo et al. 1998, 2010) during contraction from the initial radius $R_{\rm inf}$ to $R_{\rm Q}$; then one finds that

$$
\begin{aligned}
R_{\rm Q} &\approx \frac{j_{\rm inf} \, Q}{\sqrt{2} \, \sigma} \, \delta_{\rm gas}(R_{\rm Q}) \approx 6.3 \, Q \, \sigma_{60}^{-1} \, \lambda_{0.035} \, f_{\rm inf,0.6}^s \\
&\times f_{\star,0.2}^{-2/3} \, M_{\star,11}^{2/3} \, [E_z/E_{z=2}]^{-1/6} \ {\rm kpc},
\end{aligned} \tag{10}
$$

where the gas mass contrast $\delta_{\rm gas}(R_{\rm Q}) \approx 0.38$ has been computed in Appendix A taking into account the effects of adiabatic contraction. In this expression, the gas intrinsic velocity dispersion $\sigma_{60} \equiv \sigma/60 \ {\rm km \, s}^{-1}$ has been normalized to a fiducial value of $60 \ {\rm km \, s}^{-1}$ as measured in high-redshift $z \approx 2$ star-forming galaxies endowed with SFR $\gtrsim 30 \, M_\odot \ {\rm yr}^{-1}$ (see Law et al. 2009; Genzel et al. 2011; Wisnioski et al. 2015; Turner et al. 2017; Johnson et al. 2018).
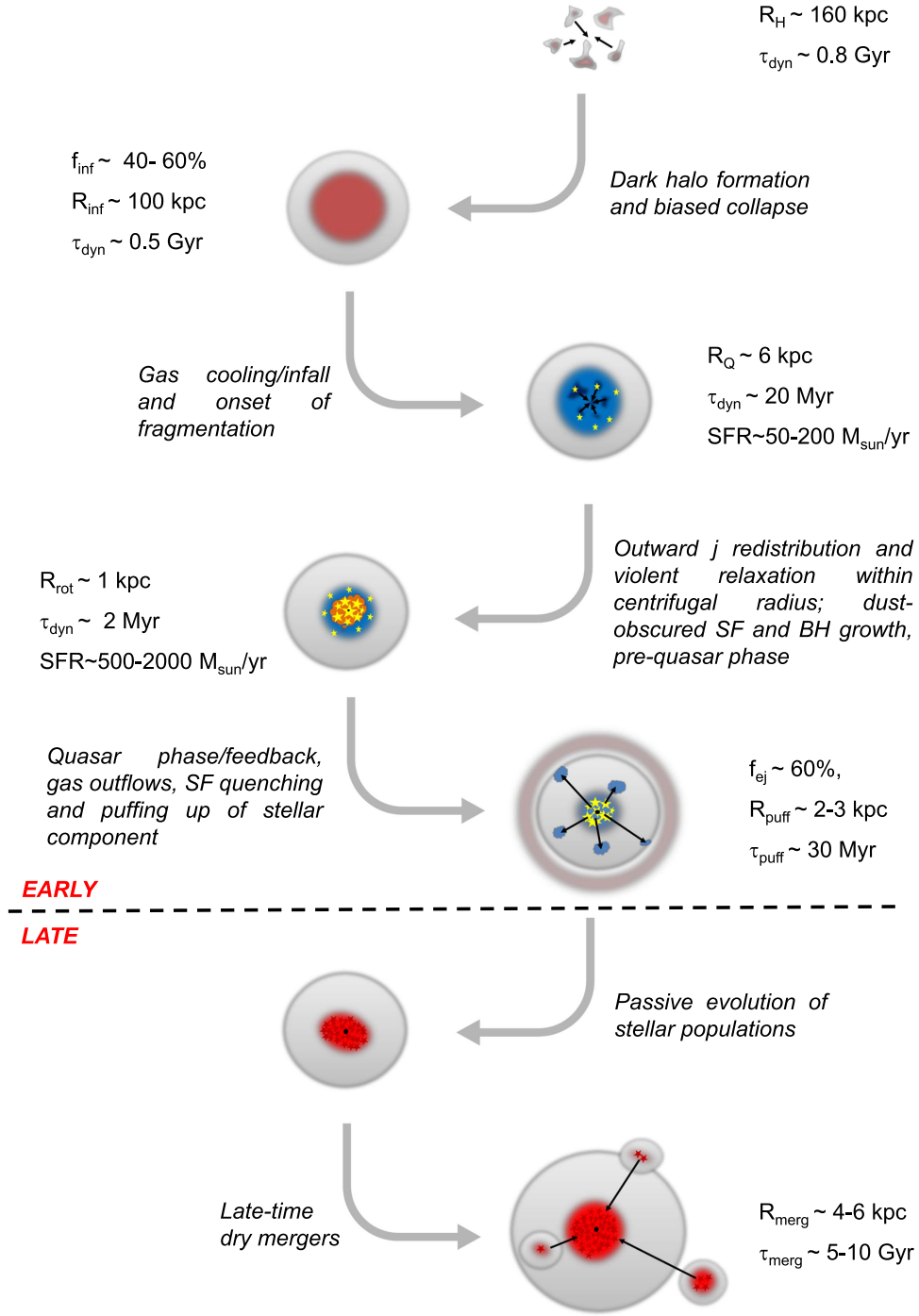
The ratio of bulk rotation velocity to random motions after Equation (9) is just

$$\left(\frac{v}{\sigma}\right)_{\rm Q} \approx 3.7 \, Q^{-1}, \tag{11}$$

and the resulting rotation velocity would approximately amount to $v_{\rm Q} \gtrsim 200 \ {\rm km \, s}^{-1}$ for a galaxy with stellar mass $M_\star \sim 10^{11} \, M_\odot$. Plainly, the above values are consistent with those obtained by conservation of specific angular momentum $j_{\rm inf}$ from $R_{\rm inf}$ to $R_{\rm Q}$, i.e., $v_{\rm Q} \simeq j_{\rm inf}/k_n \, R_{\rm Q}$, where the constant $k_n \approx 1$ applies for a thick, turbulent disk with Sérsic index $n \sim 1–2$ and $v/\sigma \gtrsim 3$ (see Romanowsky & Fall 2012; Burkert et al. 2016; Lang et al. 2017). The corresponding dynamical time at $R_{\rm Q}$ amounts to

$$
\begin{aligned}
t_{\rm dyn}(R_{\rm Q}) &\simeq \frac{\pi}{2} \sqrt{\frac{R_{\rm Q}^3}{G \, M_{\rm inf}}} \approx 2.2 \times 10^7 \, Q^{3/2} \, \sigma_{60}^{-3/2} \, \lambda_{0.035}^{3/2} \\
&\times f_{\rm inf,0.6}^{(3s-1)/2} \, f_{\star,0.2}^{-1/2} \, M_{\star,11}^{1/2} \, [E_z/E_{z=2}]^{-1/4} \ {\rm years}.
\end{aligned} \tag{12}
$$

When reaching the size $R_{\rm Q}$, the gas tends to fragment into clumps with radial velocity dispersion relative to each other of order σ. The mass of the clumps can be estimated as $M_{\rm clump} \lesssim \pi^2 \, \delta_{\rm gas}^2 \, M_{\rm inf}/16 \lesssim 10^{-1} \, M_{\rm inf}$ and amounts to several

---

[7] Adopting a standard Navarro-Frenk-White (NFW) profile (Navarro et al. 1997), the logarithmic slope of the mass distribution $M(<r) \propto r^\mu$ reads $\mu \equiv d \log M/d \log r = [cx/(1 + cx)]^2 \, [\ln(1 + cx) - cx/(1 + cx)]^{-1}$ in terms of the normalized radius $x \equiv r/R_{\rm H}$ and of the concentration parameter c. For a concentration $c \approx 4$ typical of massive galaxy halos virialized at $z \gtrsim 2$ (e.g., Bullock et al. 2001; Zhao et al. 2003), the slope μ takes on values from 0.8 to 1.2 in moving from $R_{\rm H}$ to $0.3 \, R_{\rm H}$, and can be effectively approximated with unity down to $\sim 0.4–0.6 \, R_{\rm H}$. For smaller radii, the slope progressively approaches the central value $\mu \sim 2$, which can be approximately used for $r \lesssim 0.1 \, R_{\rm H}$.

Figure 3. Cartoon illustrating the main processes that determine the size evolution of massive ($M_\star \sim 10^{11}\, M_\odot$) ETG progenitors, as discussed in the text. Typical sizes and timescales of the system throughout the evolution are also reported. The dashed horizontal line separates the early fast evolution over some 10^8 years from the late slow evolution over cosmological timescales of several Gyr.

percent of the disk gas mass (e.g., Bournaud et al. 2011; Dekel & Burkert 2014), which is consistent with observations in high-redshift galaxies (see Elmegreen et al. 2007; Guo et al. 2018) and with the outcomes of numerical simulations (see Ceverino et al. 2010; Mandelker et al. 2014, 2017; Oklopcic et al. 2017).

In principle, gravitational torques, dynamical friction, and viscosity cooperate in causing the gas and clumps to migrate toward the inner regions (see Goldreich & Tremaine 1980; Shlosman & Noguchi 1993; Noguchi 1999; Immeli et al. 2004; Dekel et al. 2009; Genzel et al. 2011; also Bournaud 2016 and references therein) over a timescale

$$t_{\mathrm{migr}}(R_Q) \simeq \frac{2.1\, Q^2}{\delta_{\mathrm{gas}}^2(R_Q)}\, t_{\mathrm{dyn}}(R_Q) \approx 3.2 \times 10^8 \text{ years.} \quad (13)$$

Although relevant for rotationally supported gas, this process close to R_Q is not crucial because the gravitational pull $G\, M_{\mathrm{tot}}(<R_Q)/R_Q^2$ appreciably exceeds the centrifugal force j_{inf}^2/R_Q^3, or equivalently, $G\, M_{\mathrm{inf}}\, R_Q > j_{\mathrm{inf}}^2\, \delta(R_Q)$ in terms of the baryonic mass contrast $\delta(R_Q) \equiv M_{\mathrm{inf}}/M_{\mathrm{tot}}(<R_Q) \approx 0.6$

computed in Appendix A. Since rotation is not sufficient to sustain gravity, gas and clumps can continue to fall in within R_Q over a dynamical time $t_{dyn}(R_Q)$ while closely maintaining their initial specific angular momentum j_{inf} (see also Danovich et al. 2015). The infall will then be halted close to the radius where the centrifugal and gravitational forces are balanced (see Section 3.2).

The issue concerning the survival of clumps is extremely complex and highly debated, with both (semi-)analytical works and hydrodynamical simulations providing contrasting results, significantly dependent on sub-grid prescriptions (see Bournaud 2016 for a comprehensive review). On one hand, it has been shown that giant clumps survive substantially intact over a few 10^8 years (e.g., Dekel & Krumholz 2013; Bournaud et al. 2014; Mandelker et al. 2017); on the other hand, a number of studies suggest that an appreciable fraction of clumps can be effectively disrupted by stellar feedback over a few 10^7 years (e.g., Murray et al. 2010; Hopkins et al. 2012; Oklopcic et al. 2017). However, the issue is alleviated in the biased collapse scenario because the relevant infall timescale $t_{dyn}(R_Q) \sim$ a few 10^7 years is also quite short (see above).

During the infall, star formation proceeds in the gas (and clumps) over a timescale t_{SFR}; observations of the correlation between star formation to gas surface density in high-redshift disks suggest values $\sim 50-100$ times longer than the dynamical time (see Elmegreen et al. 2005; Krumholz et al. 2012 and references therein), i.e.,

$$t_{SFR} \simeq (50-100) \times t_{dyn}(R_Q) \approx 1-2 \times 10^9 \text{ years.} \quad (14)$$

Energy/momentum feedback via outflows from supernovae and stellar winds is expected to regulate star formation. On spatially averaged grounds, the effects of such feedback processes are often described in terms of a mass loading factor ϵ_{out}, defined as the ratio between the outflow mass-loss rate and the SFR (e.g., Thompson et al. 2005; Feldmann 2015). Semi-analytic estimates (e.g., Lapi et al. 2014) and self-consistent hydrodynamical simulations (e.g., Hopkins et al. 2012) suggest that $\epsilon_{out} \approx 1-2$ for massive galaxies with $M_\star \gtrsim 3 \times 10^{10} M_\odot$ of interest here. Based on mass conservation arguments, a simple estimate of the ensuing average SFRs around R_Q reads

$$SFR(R_Q) \simeq \frac{1}{1 - \mathcal{R} + \epsilon_{out}} \frac{M_{inf}}{t_{SFR}} \lesssim 50-200 \, M_\odot \text{ yr}^{-1}; \quad (15)$$

here $\mathcal{R}$ is the return fraction of gaseous material from the formed stars, taking on values $\mathcal{R} \approx 0.45$ for a Chabrier IMF (e.g., Vincenzo et al. 2016).

The above approximate analytical estimates of the SFRs, sizes R_Q, and gas velocity ratios $(v/\sigma)_Q$ are consistent with the values measured via near-IR/optical observations of $z \sim 1-2$ star-forming, massive galaxies (e.g., Genzel et al. 2014; van Dokkum et al. 2015; Barro et al. 2016b). A more quantitative comparison with data is presented in Section 4.

3.2. Compaction

We have discussed above that being not rotationally supported, gas and clumps can infall within R_Q over a dynamical timescale $t_{dyn}(R_Q) \sim$ a few 10^7 years, approximately maintaining their initial specific angular momentum j_{inf}. The process can continue down to the radius R_{rot} where the

gravitational and centrifugal force balance

$$\frac{G \, M_{tot}(<R_{rot})}{R_{rot}^2} = \Omega^2 \, R_{rot} \simeq \frac{j_{inf}^2}{R_{rot}^3}. \quad (16)$$

The resulting R_{rot} can be expressed as

$$R_{rot} \approx \frac{j_{inf}^2}{G \, M_{inf}} \, \delta(R_{rot}) \approx 1.3 \, \lambda_{0.035}^2 \, f_{inf,0.6}^{2s-1}$$
$$\times f_{\star,0.2}^{-1/3} \, M_{\star,11}^{1/3} \, [E_z/E_{z=2}]^{-1/3} \text{ kpc,} \quad (17)$$

where the baryonic mass contrast is now defined as $\delta(R_{rot}) \equiv M_{inf}/M_{tot}(<R_{rot})$, with typical values $\delta(R_{rot}) \approx 0.88$ computed in Appendix A taking into account the effects of adiabatic contraction. Equation (17) implies an extremely high mass concentration of gas (and eventually of stars) inside ~ 1 kpc (see van Dokkum et al. 2014).

The kinematics at around R_{rot} will be dominated by rotation velocities $v_{rot} \simeq j_{inf}/k_n R_{rot} \gtrsim 500$ km s^{-1}, where the constant $k_n \lesssim 2$ applies to configuration with Sérsic index $n \gtrsim 2$ and $v/\sigma \gtrsim 3$ (see Romanowsky & Fall 2012; Burkert et al. 2016; Lang et al. 2017). Thus the expected ratio of rotational to random motions for the gas is

$$\left(\frac{v}{\sigma}\right)_{rot} \approx 8.9 \, \sigma_{60}^{-1} \, \lambda_{0.035}^{-1} \, f_{inf,0.6}^{1-s} \, f_{\star,0.2}^{-1/3} \, M_{\star,11}^{1/3} \, [E_z/E_{z=2}]^{1/6}. \quad (18)$$

The dynamical time at R_{rot} reads

$$t_{dyn}(R_{rot}) \simeq \frac{\pi}{2} \sqrt{\frac{R_{rot}^3}{G \, M_{inf}}} \approx 2 \times 10^6 \, \lambda_{0.035}^3 \, f_{inf,0.6}^{3s-2}$$
$$\times [E_z/E_{z=2}]^{-1/2} \text{ years.} \quad (19)$$

The Toomre parameter at R_{rot} can be estimated as $Q(R_{rot}) \simeq \sqrt{2}/\delta_{gas}(R_{rot}) \times (\sigma/v)_{rot}$ based on Equation (9); using $\delta_{gas}(R_{rot}) \approx 0.57$ as computed in Appendix A and $(v/\sigma)_{rot} \approx 9$ from Equation (18), we obtain $Q(R_{rot}) \approx 0.27$, a value that is pleasingly consistent with measurements in the central regions of high-z star-forming galaxies (see Genzel et al. 2014). The migration time at R_{rot} after Equation (13) reads

$$t_{migr}(R_{rot}) \simeq \frac{2.1 \, Q^2(R_{rot})}{\delta_{gas}^2(R_{rot})} \, t_{dyn}(R_{rot}) \approx 9.4 \times 10^5 \text{ years.} \quad (20)$$

Since the gas and clumps are rotationally supported at R_{rot}, further infall can only occur by spreading out specific angular momentum via dynamical friction and gravitational torques over the above migration time. This is mirrored in the outer placement of the stellar angular momentum with respect to the stellar mass in ETGs, as noted by Romanowsky & Fall (2012; cf. their Figure 2(b)). As $t_{migr}(R_{rot})$ is extremely short, the net result is a very rapid migration of the star-forming gas and clumps toward the inner regions.

Meanwhile, the star formation within R_{rot} occurs over a timescale

$$t_{SFR}(R_{rot}) \approx (50-100) \times t_{dyn}(R_{rot}) \approx (1-2) \times 10^8 \text{ years.} \quad (21)$$

An estimate of the ensuing average SFR is given by

$$\mathrm{SFR}(R_{\mathrm{rot}}) \simeq \frac{1}{1 - \mathcal{R} + \epsilon_{\mathrm{out}}} \frac{M_{\mathrm{inf}}}{t_{\mathrm{SFR}}(R_{\mathrm{rot}})}$$
$$\lesssim 500\text{–}2000 \, M_{\odot} \, \mathrm{years}^{-1}. \qquad (22)$$

Thus the gas and clumps around or within R_{rot} are expected to feature high SFRs, rapid metal enrichment, and dust production. Note that during the early stages of this strong star formation phase, the galaxy is expected to lie above the main-sequence relationship because the stellar mass is still growing (see Mancuso et al. 2016b). Such high SFRs can partly disrupt clumps and molecular clouds (see Murray et al. 2010) and may be subject to the Eddington limit for starbursts (e.g., Andrews & Thompson 2011; Simpson et al. 2015). All in all, we expect limited, mildly obscured SFRs in the region between R_Q and R_{rot}, and a much stronger, obscured SFR in the innermost regions within R_{rot} where most of the stellar mass is accumulated; therefore the SFRs probed by UV and far-IR data are expected to be spatially disconnected (e.g., Gomez-Guijarro et al. 2018), with the UV morphology particularly knotty and irregular (e.g., Huertas-Company et al. 2015). The above approximate analytical estimates of the SFRs, sizes R_{rot} and velocity ratios $(v/\sigma)_{\mathrm{rot}}$ are consistent with those measured via far-IR/submillimeter and CO line observations of $z \sim 1\text{–}2$ star-forming galaxies (e.g., Barro et al. 2016b, 2017; Hodge et al. 2016; Tadaki et al. 2017a; Talia et al. 2018). A more quantitative comparison with data is performed in Section 4.

As $t_{\mathrm{migr}}(R_{\mathrm{rot}}) \lesssim t_{\mathrm{dyn}}(R_{\mathrm{rot}})$ violent relaxation will operate inside R_{rot} toward setting up a new configuration in virial equilibrium that eventually results in a bulge-like structure with Sérsic index $n \gtrsim 2$. Details of this complex process can be followed only via aimed numerical simulations (e.g., Danovich et al. 2015; Zolotov et al. 2015; Zavala et al. 2016) with apt initial conditions and space/time resolutions. The final kinematic configuration of the stars is characterized by appreciable random motions, which for a bulge-like structure in virial equilibrium amounts to $\sigma_{\star,\mathrm{rot}}^2 \simeq G \, M_{\star}/\beta_n \, R_{\mathrm{rot}}$ with $\beta_n \sim 4\text{–}6$ for a Sérsic index $n \gtrsim 4$. Assuming that approximately $v_{\star,\mathrm{rot}} \lesssim v_{\mathrm{rot}} \simeq j_{\mathrm{inf}}/k_n \, R_{\mathrm{rot}}$ with $k_n \sim 2$ (see Romanowsky & Fall 2012) yields a stellar velocity ratio

$$\left(\frac{v}{\sigma}\right)_{\star,\mathrm{rot}} \lesssim \frac{\sqrt{\beta_n}}{k_n} \frac{j_{\mathrm{inf}}}{\sqrt{G \, M_{\star} R_{\mathrm{rot}}}} \approx 2 f_{\mathrm{inf},0.6}^{1/2} f_{\star,0.2}^{-1/2}, \qquad (23)$$

which is substantially lower than in the gas component; nevertheless, the system still retains appreciable rotational motions (see Barro et al. 2016a, 2017; Toft et al. 2017).

Interestingly, the compaction process described above can also create physical conditions extremely favorable to increasing the gas inflow toward the innermost regions of the galaxy (on a scale from parsec to tens of parsec) at the disposal for the formation of and rapid accretion onto a supermassive BH (e.g., Bournaud et al. 2011; Gabor & Bournaud 2013; DeGraf et al. 2017; Rujopakarn et al. 2018). This will have an important consequence for the subsequent evolution of these systems, and specifically both for the quenching of star formation and for the puffing-up of the stellar distribution (see next Section 3.3).

We note that at the end of the collapse, the central regions are expected to be strongly baryon-dominated. At first order, the radius R_b within which baryons dominate the gravitational potential can be estimated by the equality $G \, M_{\mathrm{inf}}/R_b \simeq G \, M_H(<R_b)/R_b$, which means $M_H(<R_b) \simeq [\delta(R_b)^{-1} - 1] \, M_{\mathrm{inf}}$. The result reads $R_b \approx \sqrt{[\delta(R_b)^{-1} - 1] \, 0.1 \, f_{\mathrm{inf}} \, f_b} \, R_H$ in terms of the baryonic mass contrast $\delta(R_b) \approx 0.41$ computed after taking into account adiabatic contraction (see Appendix A). Quantitatively, the baryonic-dominance radius takes on values

$$R_b \approx 18.8 \, f_{\mathrm{inf},0.6}^{1/2} \, f_{\star,0.2}^{-1/3} \, M_{\star,11}^{1/3} \, [E_z/E_{z=2}]^{-1/3} \, \mathrm{kpc}. \qquad (24)$$

We note that R_b is larger than both R_{rot} and R_Q, so that we expect a closely Keplerian rotation curve out to R_b, determined by the infall baryonic mass M_{inf}. Recent observations (see van Dokkum et al. 2015; Genzel et al. 2017) and theoretical studies (see Teklu et al. 2018) do indeed reveal such a behavior.

In the above expressions for the infall radius R_{inf}, the fragmentation radius R_Q, the rotational radius R_{rot}, and the baryon-dominance radius R_b, we have normalized the star formation efficiency $f_{\star} \approx 0.2$ and the infall fraction $f_{\mathrm{inf}} \approx 0.6$ to the values that apply for a reference mass $M_{\star} \approx 10^{11} \, M_{\odot}$. When we instead use the detailed dependencies on stellar mass/redshift according to Figures 1 and 2, we obtain the quantitative results reported in Figure 4; the halo size R_H computed according to Equation (1) is also plotted for reference. It is seen that the mass dependence is weak, especially for R_{rot}. For R_Q and R_{rot}, the mild redshift evolution in the range $z \approx 1\text{–}4$ is also illustrated.

3.3. Puffing-up by Feedbacks and Stellar Evolution

An additional process that contributes to somewhat altering the sizes of ETG progenitors is related to the outflow/ejection of a substantial fraction of gaseous material from the central region by feedback events (e.g., due to supernovae, stellar winds, and to the emission from the central supermassive BH during its quasar phase) that are thought to regulate or even quench star formation. As a consequence, the stellar component feels the change in the gravitational potential and relaxes to a more extended equilibrium configuration. In this process, usually refereed to as "puffing-up," the final size depends on the timescale τ_{exp} of gas expulsion compared with the dynamical time τ_{dyn} of the initial configuration.

For self-gravitating systems in homologous expansion, simple arguments involving energy conservation and the virial theorem can be applied. If a fraction f_{out} of the infalling mass is ejected from the central star-forming regions, then the final size R_{puff} after puffing-up is related to the initial one R_{in} by

$$\frac{R_{\mathrm{puff}}}{R_{\mathrm{in}}} \simeq \left[1 - \frac{f_{\mathrm{out}}}{1 - f_{\mathrm{out}}}\right]^{-1}, \qquad \tau_{\mathrm{exp}} \ll \tau_{\mathrm{dyn}}$$
$$\simeq 1 + \frac{f_{\mathrm{out}}}{1 - f_{\mathrm{out}}}, \qquad \tau_{\mathrm{exp}} \gtrsim \tau_{\mathrm{dyn}} \qquad (25)$$

for an abrupt (Biermann & Shapiro 1979; Hills 1980) or slow ejection (Hills 1980; Richstone & Potter 1982), respectively; comparison of the above expressions shows that a fast ejection is more effective in increasing the size, to the point that when $f_{\mathrm{out}} \gtrsim 0.5$, the system can in principle be disrupted. The corresponding velocity dispersion is expected to change from the initial σ_{in} to the final σ_{puff} value as (the quantity $\sigma^2 R/M$ is
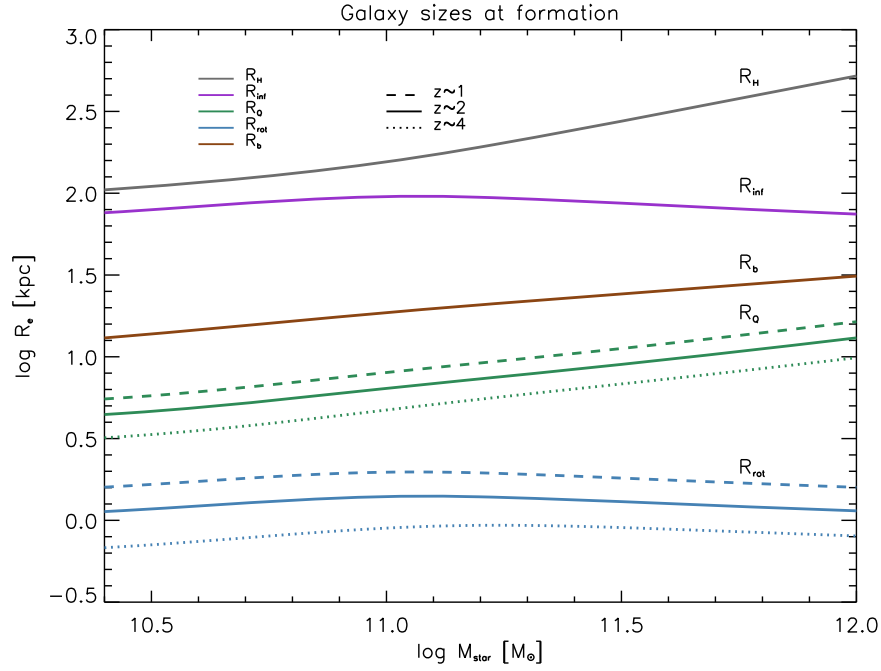
Figure 4. Relevant sizes R_e vs. stellar mass $M_\star$ for ETG progenitors at $z \approx 2$. The gray lines refer to the dark halo size $R_{\rm H}$ of Equation (1), purple lines to the infall size $R_{\rm inf}$ of Equation (6), the green line to the fragmentation size $R_{\rm Q}$ of Equation (10), the blue line to the centrifugal size $R_{\rm rot}$ of Equation (17), and the brown line to the baryonic-dominance size $R_{\rm b}$ of Equation (24). For $R_{\rm Q}$ and $R_{\rm rot}$, the solid lines show the sizes expected at redshift $z \approx 2$, the dashed lines the sizes at $z \approx 1$, and the dotted lines the sizes at $z \approx 4$.
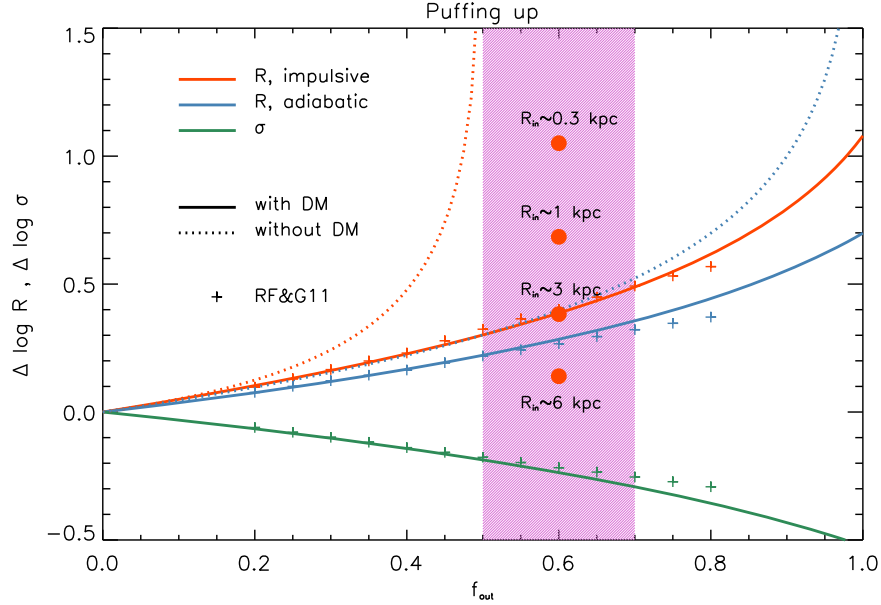
Figure 5. Size and velocity dispersion evolution due to puffing-up, in terms of logarithmic changes $\Delta \log R$ and $\Delta \log \sigma$ as a function of the fraction of outflown gas mass $f_{\rm out}$. The orange lines and symbols refer to size evolution due to an impulsive ejection, blue lines and symbols to size evolution due to an adiabatic mass loss, and green lines and symbols to velocity dispersion evolution (the impulsive and adiabatic cases practically coincide). Small crosses are the outcomes from the numerical experiments by Ragone-Figueroa & Granato (2011) in the presence of DM and for an initial size $R_{\rm in} \approx 3$ kpc, solid lines illustrates our analytic rendition, and dotted lines show the classic result for self-gravitating systems in absence of DM for reference; filled circles illustrate how the size increase for $f_{\rm out} \approx 0.6$ is affected when starting from different initial radii $R_{\rm in} \approx 6$, 3, 1, and 0.3 kpc. The shaded magenta area reports the range of outflowed mass fraction expected in ETG progenitors according to Equation (28) and Figure 2.

approximately conserved for homologous expansion)

$$\frac{\sigma_{\rm puff}^2}{\sigma_{\rm in}^2} \simeq 1 - 2 f_{\rm out}, \qquad \tau_{\rm exp} \ll \tau_{\rm dyn}$$

$$\simeq [1 - f_{\rm out}]^2 \qquad \tau_{\rm exp} \gtrsim \tau_{\rm dyn}, \qquad (26)$$

and hence to be considerably reduced, especially in the impulsive case. These simple results have been confirmed by numerical simulations of star clusters (e.g., Geyer & Burkert 2001; Boily & Kroupa 2003; Goodwin & Bastian 2006; Baumgardt & Kroupa 2007; Damjanov et al. 2009), showing that the equilibrium is recovered after 20–40 (initial) dynamical times after the ejection.

Fan et al. (2008, 2010) have been the first to suggest that this puffing-up mechanism could be enforced by massive gas outflows caused by feedback from the central supermassive BH during its quasar phase. However, the problem is more complex in galaxies because of the DM halo, and this has been studied by Ragone-Figueroa & Granato (2011) with dedicated numerical experiments. They found, as expected, that the DM halo plays a stabilizing role, with two main effects. First, the increase in size is appreciably reduced with respect to the analytic results above, but is still sizeable to a factor 1.5–4 for $f_{out} \gtrsim 0.5$ (but disruption is prevented); moreover, the increase in size is larger for smaller initial sizes because of the lower contribution of DM within the central regions where the infalling baryons reside. Useful approximated formulas for the increase in size and decrease in velocity dispersion in presence of the DM component are given by

$$\frac{R_{puff}}{R_{in}} \simeq \left(1 + \frac{\chi f_{out}}{1 - \psi f_{out}}\right) \text{ for } R_{in} \approx 3 \text{ kpc,}$$

$$\frac{R_{puff}}{R_{in}} \propto \left(\frac{R_{in}}{2.7 \text{ kpc}}\right)^{-\phi} \quad \text{for } f_{out} \gtrsim 0.4,$$

$$\frac{\sigma^2_{puff}}{\sigma^2_{in}} \simeq (1 - \omega f_{out})^2, \tag{27}$$

with $\chi = \psi^{-1} \approx 1.1$ and $\phi \approx 0.7$ for an impulsive ejection, $\chi = \psi \approx 0.8$ and $\phi \approx 0$ for a slow ejection, and $\omega \approx 0.7$ for both cases.

The ejected fraction $f_{out} \equiv M_{out}/M_{inf}$ can be estimated considering that the outflowed gas mass approximately reads $M_{out} \simeq M_{inf} - M_\star$; the resulting

$$f_{out} \simeq 1 - \frac{f_\star}{f_{inf}} \simeq 1 - \frac{Z_\star}{y_Z} \tag{28}$$

is illustrated in Figure 2 and amounts to approximately $(60 \pm 10)\%$. Most of this mass loss occurs impulsively during the star formation process as a result of feedbacks; in addition, a slower mass loss is instead related to stellar evolution, which restitutes a fraction $\mathcal{R} \approx 45\%$ of the material converted into stars (for a Chabrier IMF). These effects are both taken into account in our computation.

The net outcomes are summarized in Figure 5, where we show the evolution in size and velocity dispersion due to puffing-up after an impulsive ejection and/or adiabatic mass loss for different initial sizes R_{in} and outflowing gas fraction typical of ETG progenitors. The sizes R_{puff} and stellar velocity ratio $(v/\sigma)_{\star,puff}$ after puffing-up are consistent with those measured via near-IR/optical observations of $z \sim 1$–2 quiescent galaxies (e.g., van der Wel & van der Marel 2008; van de Sande et al. 2013; van der Wel et al. 2014; Newman et al. 2015; Hill et al. 2017; Belli et al. 2017; Glazebrook et al. 2017; Toft et al. 2017). A more detailed comparison with data is performed in Section 4.

The second result by Ragone-Figueroa & Granato (2011) concerns the timescales for equilibrium recovery, which are considerably sped up and amount to some dynamical timescales of the region containing most of the gas. Thus the galaxy is predicted to expand a short time after the gas ejection, on the order of a few to some tens of Myr (see Equations (19) and (12)). This implies that the puffing-up process must have been at work already in high-redshift $z \gtrsim 2$ compact quiescent galaxies, given that the estimated age of these systems already exceeds $\gtrsim 0.5$ Gyr (e.g., van Dokkum et al. 2009; Belli et al. 2014; van der Wel et al. 2014; Straatman et al. 2015; Kriek et al. 2016; Glazebrook et al. 2017; Toft et al. 2017). In fact, in the past years, this was an argument made against substantial puffing-up by feedback processes (Damjanov et al. 2009; Ragone-Figueroa & Granato 2011). In Section 4 we show that although compact with respect to local ETGs, $z \approx 2$ quiescent galaxies feature sizes significantly larger than for compact star-forming objects at similar redshifts, which indicates that puffing-up has already affected them. Moreover, the differential action of the puffing, which is more effective for smaller initial sizes, is found to be essential in reducing the large spread expected and observed in the size of compact star-forming systems, but not seen in the rather tight size–mass relationship of local ETGs.

We note that for an efficient, impulsive puffing-up (see Ragone-Figueroa & Granato 2011), the gas mass $M_{out} \simeq f_{out} f_{inf} M_\star/f_\star \approx (y_Z/Z_\star - 1)M_\star$ within R_{rot} must be ejected in a few dynamical times $\xi t_{dyn}(R_{rot})$ with $\xi \lesssim 5$. The resulting mass outflow rate

$$\dot{M}_{out} \approx \left(\frac{y_Z}{Z_\star} - 1\right)\frac{M_\star}{\xi \, t_{dyn}(R_{rot})} \sim 10^4 \, M_\odot \, \text{yr}^{-1} \tag{29}$$

is consistent with the values theoretically expected from feedback driven by a central supermassive BH of mass $M_{BH} \gtrsim 10^8 M_\odot$ emitting close at the Eddington rate (see Granato et al. 2004; Lapi et al. 2006, 2014; Fan et al. 2010; Beckmann et al. 2017; DeGraf et al. 2017), and with the measurements for molecular and ionized winds in powerful active galactic nuclei (e.g., Chartas et al. 2009; Prochaska & Hennawi 2009; Carniani et al. 2017; Fiore et al. 2017).

Considering the above, a specific prediction of the puffing-up scenario is that on average, quasars with high SFRs ongoing in the host should feature smaller far-IR/submillimeter sizes than counterparts whose SFR is appreciably reduced by the feedback. Such size measurements in the host galaxies of high-redshift quasars are challenging, but some data have begun to be collected by ALMA (see Venemans et al. 2016, 2017b; Decarli et al. 2017). In particular, the highest resolution observations (a factor ~ 70 better than any previous data) of a quasar at $z \sim 7.1$ with ALMA (Venemans et al. 2017b) revealed an extremely compact size $R_e \sim 1.2$ kpc of the star-forming region, as expected on the basis of our analysis (see Section 3.1). In addition, Venemans et al. (2017b) found no observational evidence of significant rotational motion inside this very central regions, i.e., $v/\sigma \ll 1$. Observations of three quasars at $z \gtrsim 6.6$ set upper limits $R_e \lesssim 4$ kpc on the size of the star-forming region, and $v/\sigma \lesssim 1.6$ to the velocity ratio. These results support the notion that in these inner regions, violent relaxation processes have been quite efficient in redistributing angular momentum outward, as assumed in our estimate of the velocity ratio at R_{rot}.

Finally, the puffing-up can contribute to smooth out the extremely peaked stellar distribution built up during the compaction and star formation processes, so increasing the effective Sérsic index of the stellar distribution toward values $n \gtrsim 4$, especially for the most massive galaxies. Such an effect will then be reinforced by late-time mass additions in the outskirts associated with dry merging (see below).
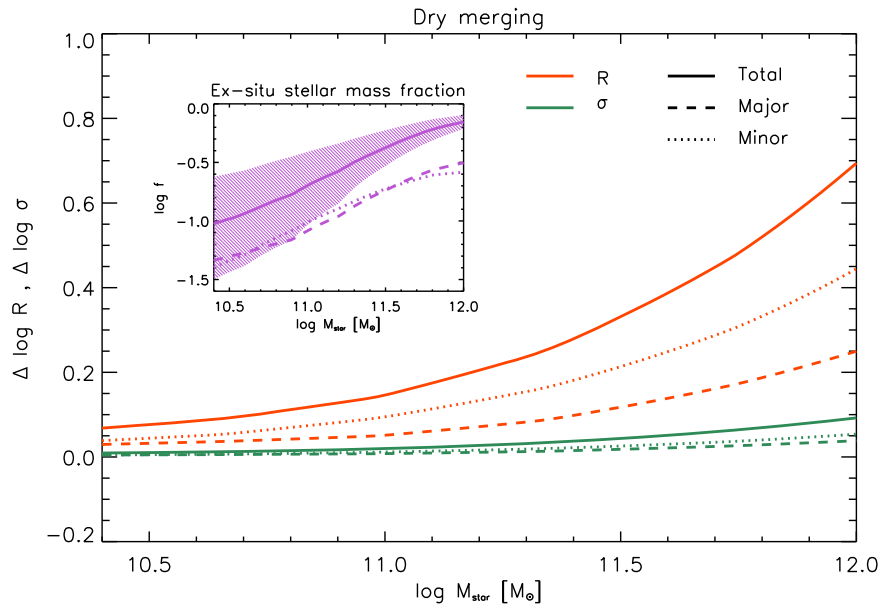
Figure 6. Size and velocity dispersion evolution due to dry mergers, in terms of logarithmic changes $\Delta \log R$ and $\Delta \log \sigma$ as a function of the final stellar mass $M_\star$. The orange lines and symbols refer to the size evolution, and the green lines to the velocity dispersion evolution. The solid lines illustrate the overall evolution, the dashed lines show the evolution due to major dry mergers, and the dotted lines represent the evolution due to minor mergers. These outcomes are based on the ex situ stellar mass fraction provided by the analysis of the *Illustris* simulations by Rodriguez-Gomez et al. (2016), which is illustrated in the inset. Solid, dashed, and dot-dashed line styles are as above for the overall, major, and minor merger fractions, respectively; the shaded area shows the variance associated with the stochasticity of the merging histories.

3.4. Growth by Dry Merging

During the late-time evolution of ETG progenitors, the size is expected to increase because of mass additions from external dry merger events.

Following Naab et al. (2009) and Fan et al. (2010), we assume that random motions are relevant in the stellar component of quiescent ETG progenitors and set $\eta \equiv M_{\rm acc}/M_{\rm in}$ and $\epsilon \equiv \sigma_{\rm acc}^2/\sigma_{\rm in}^2$, in terms of quantities referring to the accreted and initial material. The mass after merging is therefore $M_{\rm merg} = M_{\rm in}(1 + \eta)$. If $r \propto M^\kappa$, the virial theorem gives $\epsilon = \eta^{1-\kappa}$. Local ETGs have $\kappa \approx 0.56$ (Shen et al. 2003; Dutton et al. 2011; Lange et al. 2015) or even larger in the case of BCGs (Hyde & Bernardi 2009); in addition, a value $\kappa \approx 0.5$ would be implied by the Faber & Jackson (1976) relationship. From the virial theorem and the energy conservation equation, it is easily found that the fractional variations of the size and the velocity dispersion between the configurations before and after merging are

$$\frac{R_{\rm merg}}{R_{\rm in}} = \frac{(1 + \eta)^2}{1 + \eta^{2-\kappa}},$$

$$\frac{\sigma_{\rm merg}^2}{\sigma_{\rm in}^2} = \frac{1 + \eta^{2-\kappa}}{1 + \eta}. \quad (30)$$

Investigations of the fraction of close galaxy pairs and galaxies with disturbed morphologies in large catalogs (e.g., Man et al. 2016) indicate that the mass growth of massive galaxies $M_\star \gtrsim 7 \times 10^{10} M_\odot$ is constrained within a factor of ~ 1.5–2 in the redshift interval $z \sim 0.1$–2.5. Limited mass evolution $\Delta \log M_\star \approx 0.16 \pm 0.04$ is also confirmed for a sample of quiescent galaxies at redshift $z \sim 1.6$ by Belli et al. (2014). Recently, Buitrago et al. (2017) have explored the assembly of the outermost regions of the most massive galaxies with $M_\star \gtrsim 5 \times 10^{10} M_\odot$, finding that the fraction of stellar

mass stored in the outer envelopes amounts to about 30% locally and decreases to 15% at $z \lesssim 0.65$ and to 3.5% at $z \sim 2$.

The analysis of the *Illustris* simulations by Rodriguez-Gomez et al. (2015, 2016) has addressed the median fraction $f_{\rm merg}$ of ex situ mass added by dry mergers for a given final stellar mass. The outcome is illustrated (together with the variance associated to the stochasticity in merging history) in the inset of Figure 6. The contribution by dry mergers is negligible for current stellar masses $M_\star \lesssim 3 \times 10^{10} M_\odot$ and increases appreciably for the most massive galaxies with $M_\star \gtrsim 3 \times 10^{11} M_\odot$, where both major and minor mergers play a relevant role; a residual small fraction of accreted mass is in the form of stars stripped from surviving galaxies that do not cause size evolution since the required timescales are too long (see Boylan-Kolchin et al. 2008).

Based on these numerical results, we adopt an average mass ratio $\langle \eta_{\rm M} \rangle \approx 1/4$ and $\langle \eta_{\rm m} \rangle \approx 1/10$ for major (suffix "M") and minor (suffix "m") mergers and compute the overall average number $\langle N_{\rm m,M} \rangle$ of major and minor mergers from $z \approx 2$ to the present time as

$$\langle N_{\rm m,M} \rangle = \frac{\log[1 + f_{\rm m,M}/(1 - f_{\rm merg})]}{\log[1 + \langle \eta_{\rm m,M} \rangle]}; \quad (31)$$

finally, we repeatedly apply Equations (30) to each merger event to obtain the global evolution in size and velocity dispersion at a given final stellar mass. The outcomes are plotted in the main panel of Figure 6; the velocity dispersion evolution is mild at all masses, while the size evolution is substantial for final stellar masses $M_\star \gtrsim 10^{11} M_\odot$ (see Shankar et al. 2013, 2014). These conclusions are stable against reasonable variations of the average mass ratios.

The size $R_{\rm merg}$ and stellar velocity ratio $(v/\sigma)_{\star,\rm merg}$ after dry merging are consistent with those measured via near-IR/optical observations of local ETGs (e.g., Shen et al. 2003; Cappellari
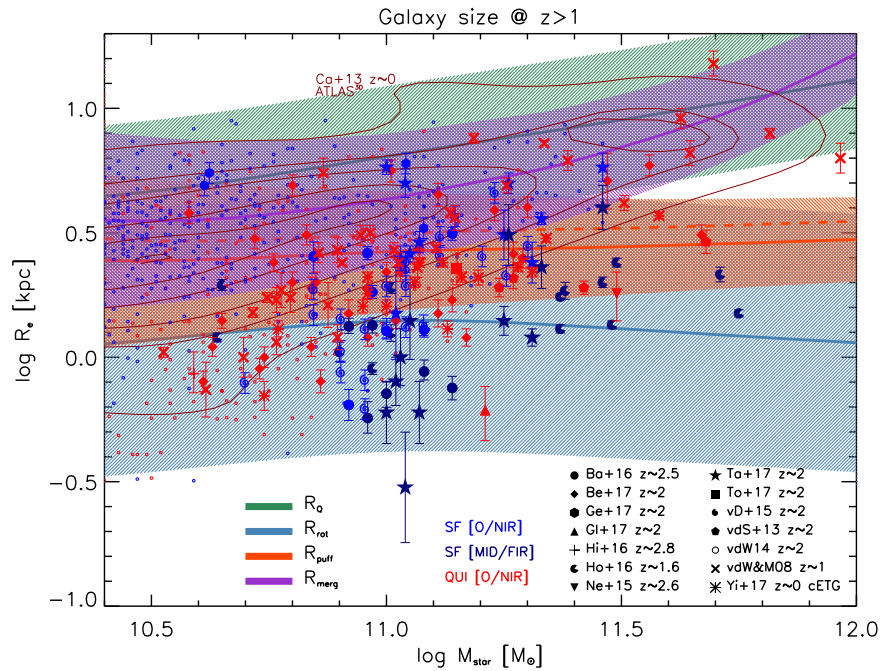
Figure 7. Size R_e vs. stellar mass $M_\star$ relationship. The colored lines with shaded areas illustrate the size–mass relationship and the associated scatter expected along the evolution of ETG progenitors: the green line refers to the fragmentation size R_Q of Equation (10), the blue line refers to the centrifugal size R_{rot} of Equation (17), the orange line to the size R_{puff} of Equation (27) after puffing-up (solid for impulsive puffing due to feedbacks and dashed for adiabatic puffing due to stellar evolution), and the magenta line to the final size R_{merg} after dry merging. Data are from Barro et al. (2016a; circles) at $z \sim 2.5$, Belli et al. (2017; diamonds) at $z \sim 2$, Genzel et al. (2017 hexagons) at $z \sim 2$, Glazebrook et al. (2017; triangles) at $z \sim 2$, Hill et al. (2017; plus sign) at $z \sim 2.8$, Hodge et al. (2016; pacmans) at $z \sim 1.6$, Newman et al. (2015; reverse triangles) at $z \sim 2.6$, Tadaki et al. (2017a; stars) at $z \sim 2$, Toft et al. (2017; squares) at $z \sim 2$, van Dokkum et al. (2015; spirals) at $z \sim 2$, van de Sande et al. (2013; pentagons) at $z \sim 2$, van der Wel & van der Marel (2008; crosses) at $z \sim 1$, van der Wel et al. (2014; dots) at $z \sim 2$, and Yildirim et al. (2017; asterisks) at $z \sim 0$ for compact ETGs. Blue points refer to star-forming galaxies (light blue for sizes inferred from optical/near-IR observations, deep blue points for sizes inferred from mid-/far-IR observations), and red points refer to quiescent galaxies. The dark red contours report the size distributions of local ETGs from the ATLAS³ᴰ survey by Cappellari et al. (2013).

et al. 2013; Cappellari 2016 and references therein). A more detailed comparison with data is performed in Section 4.

4. Results and Comparison with Data

In Figures 7 and 8 we illustrate the size versus stellar mass relationships expected throughout the evolution of ETG progenitors; in particular, Figure 7 offers a unified picture, while Figure 8 dissects the evolution in various stages. First, we focus on star-forming progenitors. The green line refers to the fragmentation size R_Q of Equation (10), while the blue line shows the rotational radius R_{rot} of Equation (17). The shaded areas show the corresponding dispersions, mainly determined by that in the halo spin parameter λ; it is evident that the scatter in $R_{rot} \propto \lambda^2$ is substantially larger than in $R_Q \propto \lambda$, which is due to its stronger dependence. According to the discussion in Section 3, we expect that in between the size R_Q and R_{rot}, the typical SFRs $\lesssim 50$–$200 \, M_\odot \, \mathrm{yr}^{-1}$ are moderate and dust obscuration is mild or negligible, so that these regions can be probed by near-IR/optical observations; conversely, we expect that around or within R_{rot}, the SFRs $\lesssim 500$–$2000 \, M_\odot \, \mathrm{yr}^{-1}$ are strong and dust obscuration is heavy, so that these regions are hidden from near-IR/optical observations and can only be probed via mid/far-IR data. As an end-product of significantly higher SFRs in the central regions $\lesssim 1$ kpc with respect to the outskirts, a very high stellar mass concentration will result, as indicated by observations of $z \sim 2$ massive quiescent galaxies (see van Dokkum et al. 2014).

Our expectations are consistent with the measured sizes of $z \approx 2$ star-forming galaxies (see van Dokkum et al. 2015;

Barro et al. 2016b, 2017; Hodge et al. 2016; Genzel et al. 2017; Tadaki et al. 2017a; Massardi et al. 2018; Talia et al. 2018). Specifically, sizes inferred from near-IR/optical data (light blue symbols) are seen to be located in between R_Q and R_{rot}, while sizes inferred from mid-/far-IR data (dark blue symbols) lie around and within R_{rot}. For the samples by Barro et al. (2016b) and Tadaki et al. (2017a), we have reported both the near-IR/optical size measured from data obtained with the *Hubble Space Telescope* (*HST*) and the far-IR sizes from ALMA data for the very same objects, to show that the far-IR sizes are typically a factor 2–4 smaller than the near-IR/optical ones. High-resolution, multiband observations (e.g., Negrello et al. 2014; Massardi et al. 2018) of strongly lensed dusty star-forming galaxies have also highlighted a clear spatial segregation between the UV and far-IR emissions, with the latter being substantially more concentrated. Note that the extremely large dispersion in the data points for star-forming galaxies is in part spuriously due to this difference between near-IR and far-IR sizes; however, even when considering data with homogenous selection, the dispersion remains substantial, in agreement with our expectation regarding the scatter on R_Q and R_{rot}.

We note that it has been reported in the literature that the sizes of $z \sim 2$ star-forming galaxies are of the same order or even larger than that of quiescent galaxies at similar redshift (e.g., van der Wel et al. 2014; Straatman et al. 2015). However, this conclusion was based on sizes determined via near-IR/optical data and was therefore fundamentally flawed by an observational bias. For quiescent galaxies, which are essentially dust free, the near-IR size is a robust estimate of the
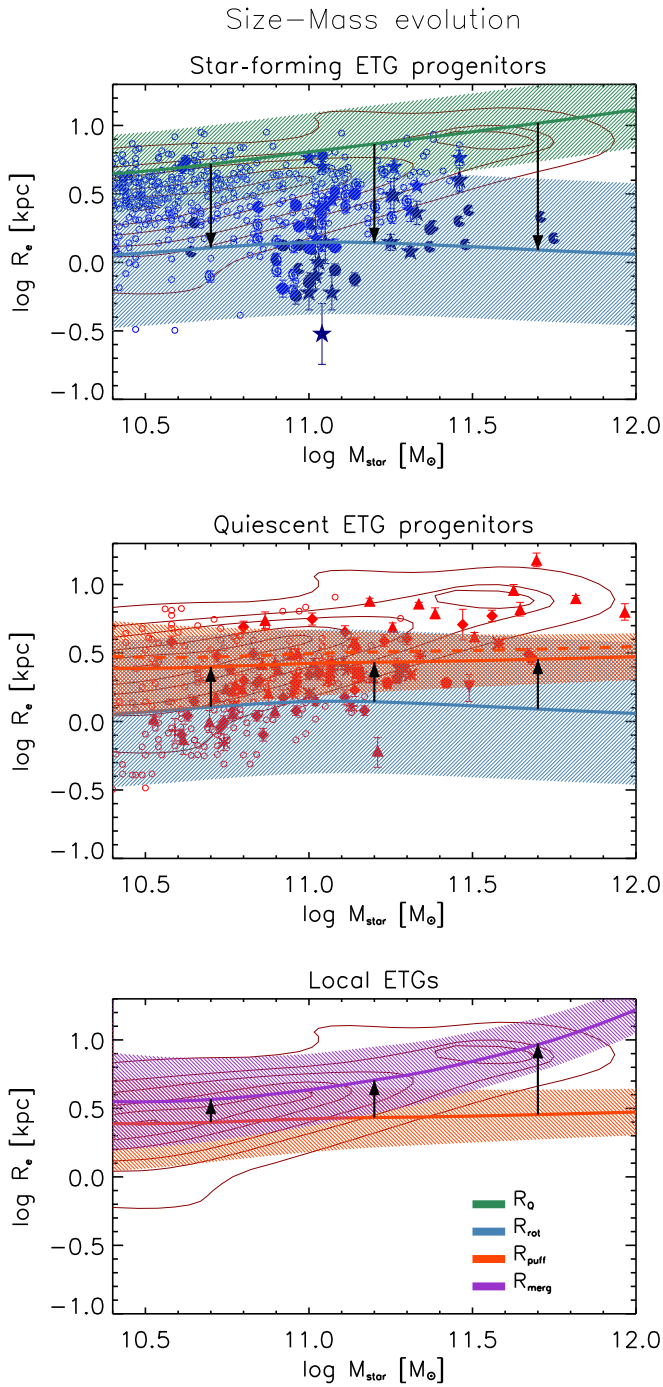
Figure 8. Dissected evolution of the size R_e vs. stellar mass $M_\star$ relationship for massive ETGs: the top panel refers to star-forming ETG progenitors, the middle panel to quiescent ETG progenitors, and the bottom panel to late-time evolution toward local ETGs. As in the previous figure, line styles and shaded areas refer to relevant sizes (and their associated dispersions), with the black arrows illustrating the evolution from one to another. Colored symbols show various data sets at high-redshift as in the previous figure; the contours refer to the local relationship, plotted for reference in each panel.

radius containing most of the stellar mass; in contrast, for strongly star-forming galaxies, which are heavily dust obscured in the inner regions, the near-IR size substantially over-estimates the true radius at which most of the star formation takes place and most of the stellar mass is accumulated. Taking into account high-resolution far-IR/submillimeter observations (e.g., taken with ALMA), it appears evident from the data

collection in Figure 7 that the sizes of star-forming galaxies are appreciably smaller than those of quiescent galaxies.

On the basis of Section 3.3, we expect that after $\lesssim$ Gyr, the star formation in ETG progenitors is quenched by some feedback processes (presumably the activity of the central supermassive BH during its powerful quasar phase) and that the sudden ejection of a substantial amount of matter (see Figure 2) from the central region puffs up the stellar component to a new, more extended equilibrium configuration (cf. Figure 5). The resulting size $R_{\rm puff}$ illustrated in Figures 7 and 8 as an orange solid line (the orange dashed line includes puffing-up by adiabatic mass loss during passive evolution) is in agreement with the measured size of high-z massive quiescent galaxies (van der Wel & van der Marel 2008; van de Sande et al. 2013; Hill et al. 2017; Belli et al. 2017; Glazebrook et al. 2017; Toft et al. 2017). Interestingly, even the sizes of local compact quiescent galaxies measured by Yildirim et al. (2017) agree well with the predicted $R_{\rm puff}$. These are galaxies that remained compact until the present because of a lack in size evolution due to late-time dry merger events; moreover, they are known to host extremely massive BHs at their centers that may have caused a strong puffing-up at the peak time of their activity.

As discussed in Section 3.3 and illustrated in Figure 5, the puffing-up mechanism is more effective in galaxies with a smaller initial radius (see Equation (27)); thus the scatter associated with $R_{\rm puff}$ is found to be considerably smaller (orange shaded area) than that in $R_{\rm rot}$. This is remarkable because the scatter in $R_{\rm rot} \propto \lambda^2$, mainly determined by that in the spin parameter λ (see above), would have been far too large with respect to that observed in the size–mass relationships of local ETG; puffing-up offers a viable mechanism to reduce the scatter in $R_{\rm rot}$ along the evolutionary sequence of ETG progenitors.

The last step in such an evolution involves the addition of mass via dry merger events, as discussed in Section 3.4. We exploit the outcome reported in Figure 6 for realistic mass growth histories from simulations to evolve the size of (quiescent) ETG progenitors toward the present. The resulting size $R_{\rm merg}$ is illustrated in Figures 7 and 8 as a magenta line; the associated scatter, shown as a magenta shaded area, is somewhat increased with respect to that in $R_{\rm puff}$; this is because of the variance in the mass fraction added by dry mergers (see inset of Figure 6), which reflects the stochasticity in the galaxy merging histories.

The average size $R_{\rm merg}$ and its dispersion agree fairly well with the size versus mass relationship of local ETGs as measured by the ATLAS$^{\rm 3D}$ survey (dark red contours; Cappellari et al. 2013). We note that the final sizes of ETGs are incidentally not so different from the initial fragmentation size R_Q of their progenitors, which as discussed above is basically the size inferred via near-IR/optical observations; without the recent size measurements from far-IR/submillimeter data it would have been very difficult to envisage a self-consistent evolutionary path for ETG progenitors in the size versus mass diagram.

We now consider the kinematic evolution of ETG progenitors. In Figure 9 we illustrate the ratio v/σ of the rotational velocity v to the velocity dispersion σ expected along the evolutionary history. Focusing first on the star-forming phase of ETG progenitors, we expect that the gas velocity dispersion $\sigma \approx 30\text{–}80\,{\rm km\,s^{-1}}$ is mainly set by turbulent
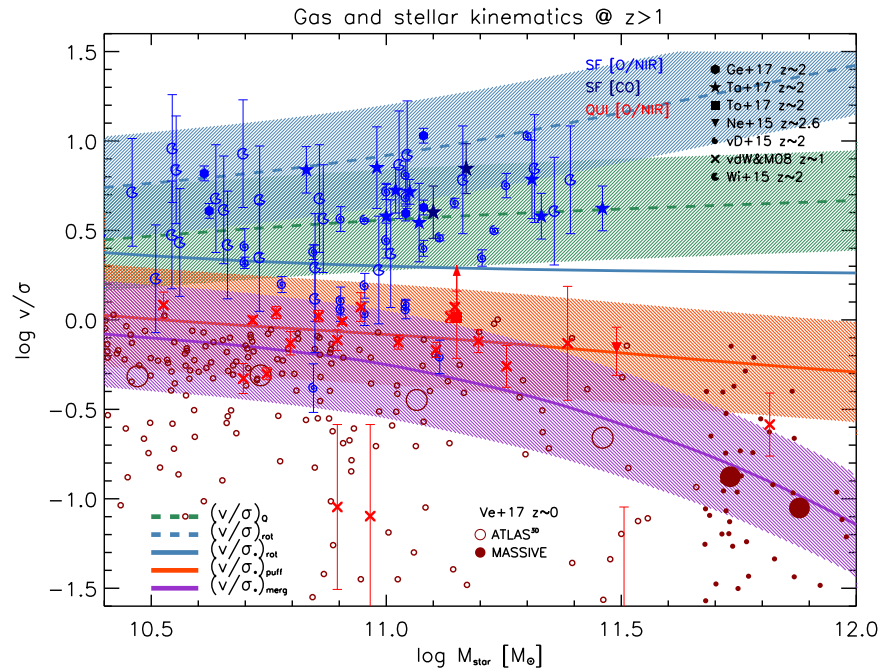
Figure 9. Ratio v/σ between rotation to dispersion velocity vs. stellar mass $M_\star$. The colored lines with shaded areas illustrate the average relationship and scatter expected along the evolution of ETG progenitors: the green dashed line refers to the gas velocity ratio $(v/\sigma)_Q$ at the fragmentation radius R_Q, the blue dashed line to the gas velocity ratio $(v/\sigma)_{\rm rot}$ at the centrifugal size $R_{\rm rot}$ and the blue solid line is the ratio $(v/\sigma)_{\star,\rm rot}$ at the same radius for the stellar component (corresponding shaded area not plotted for clarity), the orange solid line to the stellar velocity ratio $(v/\sigma)_{\star,\rm puff}$ at the radius $R_{\rm puff}$ after puffing-up, and the magenta solid line to the stellar velocity ratio $(v/\sigma)_{\star,\rm merg}$ at the final radius $R_{\rm merg}$ after dry merging. Data are from Genzel et al. (2017; hexagons) at $z \sim 2$, Tadaki et al. (2017a, 2017b; stars) at $z \sim 2$, Toft et al. (2017; squares) at $z \sim 2$, Newman et al. (2015; reverse triangles) at $z \sim 2.6$, van Dokkum et al. (2015; spirals) at $z \sim 2$, van der Wel & van der Marel (2008; crosses) at $z \sim 1$, and Wisnioski et al. (2015; pacmans) at $z \sim 2$. Blue points refer to star-forming galaxies (light blue for kinematics inferred from optical/near-IR observations, deep blue for kinematics inferred from CO observations), and red points refer to quiescent galaxies. The dark red circles (small circles for individual objects and large circles for the average) illustrate the $(v/\sigma)_\star$ distributions of local ETGs from the ATLAS$^{\rm 3 D}$ (open circles) and MASSIVE (filled circles) surveys as reported by Veale et al. (2017).

motions in the interstellar medium, while the rotational velocity is associated with the angular momentum $j_{\rm inf}$ of the gas infalling in the central regions. The green line in Figure 9 shows our expectation at the fragmentation size R_Q, which on the basis of Equation (11) amounts to a velocity ratio $(v/\sigma)_Q \gtrsim 3$, weakly increasing with stellar mass. Our predicted ratio, also taking into account the associated dispersion (green shaded area), pleasingly agrees with the current observational estimates for star-forming galaxies at $z \approx 1-2$ by Genzel et al. (2017), Di Teodoro et al. (2016), Johnson et al. (2018), Tadaki et al. (2017a), van Dokkum et al. (2015), and Wisnioski et al. (2015). These dynamical observations have all been performed using near-IR/optical facilities (e.g., KMOS), and as such can reliably probe the v/σ ratio for the gas only in galaxy regions where dust obscuration is not substantial, i.e., around R_Q.

On the other hand, we expect that in the inner regions around $R_{\rm rot}$, where heavily dust-enshrouded star formation is ongoing and most of the stellar mass accumulates, the velocity ratio of the gas increases appreciably to values $(v/\sigma)_{\rm rot} \lesssim 10$; the reason is that in the compaction from R_Q to $R_{\rm rot}$ the rotational velocity v increases moderately as the specific angular momentum is nearly conserved. Preliminary data from ALMA CO observations in several objects (Tadaki et al. 2017b) appear consistent with this prediction. On the other hand, the $(v/\sigma)_{\star,\rm rot}$ ratio associated with the stellar component is expected to be substantially lower because within $R_{\rm rot}$, violent relaxation processes enforce a high stellar velocity dispersion $\sigma_\star$; in the final configuration after relaxation, random motions must sustain the inner gravitational potential dominated by the stellar mass. The outcome after Equation (23) is a ratio

$(v/\sigma)_{\star,\rm rot} \sim 1 - 2$ that is nearly constant with stellar mass. This is a specific prediction to be tested with high-resolution spectroscopic observations, although the strong obscuration makes the task extremely challenging while star formation is still ongoing.

The subsequent step in the evolution of ETG progenitors involves the quenching of the star formation by feedback processes and the associated puffing-up. The size is increased from $R_{\rm rot}$ to $R_{\rm puff}$ by a factor a few, and as a consequence, the rotational velocity is expected to decrease appreciably, while the stellar velocity dispersion is only mildly affected (see the last of Equations (27)). The resulting velocity ratio $(v/\sigma)_{\star,\rm puff}$ for the stellar component is illustrated in Figure 9 by the orange line. This is in agreement with the dynamical measurements for quiescent galaxies by Newman et al. (2015) at $z \sim 2$, by van der Wel & van der Marel (2008) at $z \sim 1$, and by Yildirim et al. (2017) for local compact ETGs that are thought to reflect the behavior of high-redshift quiescent counterparts.

During the late-time evolution of ETG progenitors, we expect that the size is increased appreciably by dry merger events, especially for the most massive galaxies. From the dynamical point of view, the velocity dispersion is mildly affected (see Equation (30) and Figure 6), while the rotational velocity is reduced both due to the increase in size and to partial spin cancellation during encounters (e.g., Maller et al. 2002; D'Onghia & Burkert 2004; Romanowsky & Fall 2012); for typical mass additions of a factor $\lesssim$1.5–2 as occur for massive galaxies (see Figure 6), the specific angular momentum loss is around 40% (see Shi et al. 2017). All in all, we expect the velocity ratio $(v/\sigma)_{\star,\rm merg}$ to decrease, and especially

so for the more massive galaxies that experience on average more mass additions by dry mergers. The detailed outcome based on the dry merger histories extracted from numerical simulations (see Section 3.4 and Figure 6) is illustrated by the magenta line in Figure 9; it agrees well with the dynamical measurements by Veale et al. (2017) from the ATLAS^{3D} and the MASSIVE surveys (individual data are shown by small circles and average values by large circles) marginalized over ellipticity. In passing, it is quite interesting that the stellar velocity dispersion $\sigma_\star$ is only mildly affected both by puffing-up and by late-time dry mergers; this may be contribute to explaining the tightness and weak evolution of the BH mass versus $\sigma_\star$ relationship (e.g., Shankar et al. 2009; Aversa et al. 2015).

In Figure 10 we present the relationship between specific angular momentum and stellar mass during the evolution of ETG progenitors. The angular momentum has been rescaled by the factor $E^{1/6}(z)$ to remove the trivial redshift evolution associated with the halo angular momentum j_H, see Equation (3). The green solid line and shaded area show the angular momentum $j_{\rm inf}\, E_{z=2}^{1/6}$ associated with the infalling gas in $z \sim 2$ star-forming galaxies, as expected in the biased collapse scenario for an infalling gas fraction from Equation (5) and Figure 2. Remarkably, our expectation for $j_{\rm inf}$ agrees well in normalization and dispersion with the measurements for $z \sim 1$–2 star-forming galaxies by Burkert et al. (2016), Tadaki et al. (2017a, 2017b), Swinbank et al. (2017), and van Dokkum et al. (2015).

The solid magenta line with the shaded area shows the stellar specific angular momentum $j_\star\, E_{z=0}^{1/6}$ expected at $z \approx 0$ after dry merger evolution, which implies both an increase in stellar mass and a 40% angular momentum loss with respect to the initial $j_{\rm inf}$ by partial spin cancellation during encounters (see Section 3.4); for comparison, the angular momentum $j_\star\, E_{z=0}^{1/6}$ at $z \approx 0$ with no momentum loss (but still including the increase in stellar mass) is shown as a dashed magenta line. The outcome for $j_\star$ is in reasonable agrement (given the large scatter) with the data for quiescent galaxies at $z \sim 1$–2 by Toft et al. (2017), Newman et al. (2015), and van der Wel & van der Marel (2008), and for local ETGs by Romanowsky & Fall (2012).

5. Discussion and Conclusions

In this paper we have provided a holistic view on the typical size and kinematic evolution of massive ETGs that encompasses their high-z star-forming progenitors, their high-z quiescent counterparts, and their configurations in the local Universe.

Our investigation covers the main processes playing a relevant role in the cosmic evolution of ETGs. Specifically, their early fast evolution comprises biased collapse of the low angular momentum gaseous baryons located in the inner regions of the host DM halo; cooling, fragmentation, and infall of the gas down to the radius set by the centrifugal barrier; further rapid compaction via clump/gas migration toward the galaxy center, where strong heavily dust-enshrouded star formation activity takes place and most of the stellar mass is accumulated; ejection of substantial amount of gas from the inner regions by feedback processes and dramatic puffing-up of the stellar distribution. In the late slow evolution, passive aging of stellar populations and mass additions by dry merger events occur.

We have described these processes relying on prescriptions inspired by basic physical arguments and by numerical simulations to derive new analytical estimates of the relevant sizes, timescales, and kinematic properties for individual galaxies during their evolution. Then we have obtained quantitative results as a function of galaxy mass and redshift and have compared them to recent observational constraints on half-light size R_e, on the ratio v/σ between rotation velocity and velocity dispersion (for gas and stars), and on the specific angular momentum $j_\star$ of the stellar component; we have found an overall good consistency with the available multiband data in average values and dispersion both for local ETGs and for their $z \sim 1$–2 star-forming and quiescent progenitors.

Our main conclusions are listed below.

1. In high-z progenitors of ETGs, the biased collapse of a fraction $f_{\rm inf} \approx 0.4$–0.6 of the baryons initially present in the halo and enclosed within the size $R_{\rm inf} \lesssim 10^2$ kpc sets the timescale $t_{\rm dyn}(R_{\rm inf}) \approx$ some 10^8 years driving the subsequent evolution. Cooling and fragmentation of the infalling gas occurs on a size $R_Q \lesssim 10$ kpc where a gaseous clumpy, unstable disk with appreciable rotational motions $(v/\sigma)_Q \gtrsim 3$ is formed. Dynamical friction, gravitational torquing, and viscosity would imply migration timescales of a few 10^8 years for the gas and the clumps; in the biased collapse scenario, this process in not crucial around R_Q, since the low specific angular momentum of the gas is not sufficient to sustain the gravitational pull. As a consequence, gas and clumps infall over a dynamical timescale of few tens of Myr, approximately maintaining their initial specific angular momentum. During the infall, gas and clumps are expected to feature moderate SFR $\lesssim 50$–$200\, M_\odot$ yr^{-1}, resulting in mild metal enrichment and dust obscuration. Near-IR/optical observations in $z \sim 1$–2 star-forming galaxies indeed measure size and kinematic properties consistent with our expectations. See Sections 3.1, 4, and Figures 4 and 7–9 for more details.

2. The infall of gas and clumps toward the inner regions halts at around the radius $R_{\rm rot} \lesssim 1$ kpc where gravity and centrifugal support are balanced; at this radius, the gas kinematics is largely dominated by rotational velocities of several hundreds km s^{-1} corresponding to $v/\sigma \lesssim 10$, and the disk fragmentation is enhanced by the further decrease of the Toomre parameter $Q \lesssim 0.3$. The size $R_{\rm rot} \propto \lambda^2$ strongly depends on the spin parameter λ of the host DM halo and therefore features a large dispersion around 0.5 dex. Further collapse of the gas is made possible by transfer of angular momentum toward the outer regions via dynamical friction over a migration timescale $\lesssim 10^6$ years. Meanwhile, strong SFRs $\lesssim 500$–2000 $M_\odot$ yr^{-1}, substantial metal enrichment, and dust obscuration are expected to take place within $R_{\rm rot}$. Violent relaxation processes drive the system toward a bulge-like configuration in virial equilibrium; finally, high stellar masses $M_\star \gtrsim$ from several to many $10^{10}\, M_\odot$ are accumulated within $\lesssim 1$ kpc, with appreciable residual rotational support $(v/\sigma)_{\star,\rm rot} \sim 1$–2 in the stellar component. In fact, size and kinematic data from far-IR/submillimeter observations are consistent with our predictions. See Sections 3.2, 4, and Figures 4 and 7–9 for more details.

3. After several 10^8 years, the star formation process is expected to be quenched by energy feedback from stellar
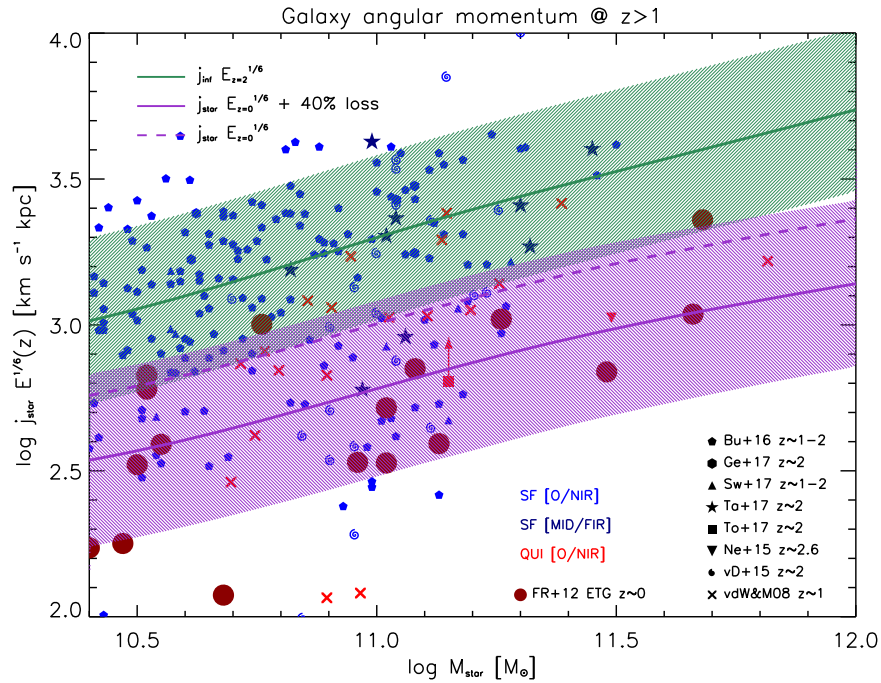
Figure 10. Specific angular momentum vs. stellar mass. The colored lines with shaded areas illustrate the average relationship and scatter expected during the evolution of ETG progenitors: the green line illustrates the specific angular momentum $j_{inf} E_{z=2}^{1/6}$ of the infalling gas at $z \sim 2$; and the magenta lines show the stellar angular momentum $j_\star E_{z=0}^{1/6}$ at $z \sim 0$, with the solid line including an angular momentum loss of 40% due to late-time dry mergers and the dashed line referring to no angular momentum loss (only mass addition and redshift scaling included). Data are from Burkert et al. (2016; pentagons) at $z \sim 1$–2, Genzel et al. (2017; hexagons) at $z \sim 2$, Swinbank et al. (2017; triangles) at $z \sim 1$–2, Tadaki et al. (2017a, 2017a; stars) at $z \sim 2$, Toft et al. (2017; squares) at $z \sim 2$, Newman et al. (2015; reverse triangles) at $z \sim 2.6$, van Dokkum et al. (2015; spirals) at $z \sim 2$, and van der Wel & van der Marel (2008; crosses) at $z \sim 1$. Blue points refer to star-forming galaxies (light blue for optical/near-IR observations, deep blue for mid-/far-IR observations), and red points refer to quiescent galaxies. The large dark red circles report the angular momentum distribution of local ETGs from Romanowsky & Fall (2012).

winds/supernovae or, most likely, from the central supermassive BH during its powerful quasar phase: a high-z, massive quiescent galaxy results. During the quenching, a substantial fraction $f_{out} \approx 0.5$–0.7 of the infalling gas is ejected from the inner regions; this enforces a puffing-up of the stellar distribution to a size $R_{puff} \sim 3$–5 kpc. This is a factor of a few to several larger than R_{rot}. Even more relevantly, due to the presence of DM, the puffing-up process is more pronounced in galaxies that initially were more compact; as a consequence, the dispersion in the size R_{puff} is considerably smaller than that in the initial size R_{rot}. As a consequence of the size expansion, the mass concentration in the central region $\lesssim 1$ kpc of quiescent galaxies is somewhat decreased with respect to that of their star-forming progenitors. The puffing-up process mildly affects the stellar velocity dispersion, while the rotational velocity is appreciably decreased because of the expansion in size, to yield a velocity ratio $(v/\sigma)_{\star,puff} \gtrsim 0.5$. The current near-IR/optical data on sizes and kinematics of $z \sim 1$–2 massive quiescent galaxies are consistent with such findings. See Sections 3.3, 4, and Figures 5 and 7–9 for more details.

4. In the subsequent passive evolution toward the present time, mass additions by dry merging events can alter the size and kinematics of quiescent galaxies, especially so for massive systems. The final size R_{merg} for the most massive galaxies is increased by factor around 2–3 from $z \sim 2$ to 0, while the dispersion is somewhat enhanced because of the variance in merging histories. Meanwhile, the stellar velocity ratio $(v/\sigma)_{\star,merg}$ is decreased

somewhat, mainly because the rotation velocity is lowered by the increase in size and by a 40% angular momentum loss via partial spin cancellation during encounters. The outcomes of our analysis are consistent with the observed size R_e and $(v/\sigma)_\star$ distribution of local ETGs, both in average values and dispersion. See Sections 3.4, 4, and Figures 6 and 7–9 for more details.

5. We predict, and found agreement in the available data, that the specific angular momentum of ETG progenitors is close to the value dictated by the biased collapse of a fraction $f_{inf} \approx 0.4$–0.6 of the initial baryons. Local ETGs reflect the same momentum but for minor losses due to late-time dry mergers. See Section 3, 4, and Figure 10 for more details.

It is interesting to compare our findings to the outcomes of recent hydro-cosmological simulations. For size and kinematics, Zolotov et al. (2015) find that star-forming progenitors of galaxies with final mass $M_\star \sim 10^{11} M_\odot$ featured small sizes $R_e \lesssim$ kpc and rotational to random velocity ratios $v/\sigma \gtrsim 2$ in the gaseous and $(v/\sigma)_\star \sim 1$ in the stellar component. More recently, both Genel et al. (2018) analyzing the *IllustrisTNG* simulation and Furlong et al. (2017) analyzing the *EAGLE* simulation confirm that the progenitors of local massive quiescent galaxies are characterized by small sizes $\lesssim$ a few kpc during their star formation phase, while after quenching they experience a substantial size growth due to outward stellar migration, renewed star formation, and mass addition from dry mergers.

A clear prediction of recent simulations is that on average, ETG progenitors evolve toward a low angular momentum state

by various processes, such as angular momentum redistribution during compaction, early star formation quenching by feedbacks, and dry mergers. In their *EAGLE* simulations, Zavala et al. (2016) find a strong relation between the specific angular momentum of the stars and that of the host DM halo in the inner star-forming region. Lagos et al. (2017) use the same simulation suite and envisage that an early star formation quenching plus dry mergers can be rather effective in producing galaxies with low specific angular momentum. These studies both indicate that massive halos with a turnaround epoch $z \gtrsim 2$ typically host central galaxies featuring old stellar populations with low specific angular momentum. On the other hand, the same simulations suggest that halos with a late formation/turnaround epoch $z \lesssim 1$ tend to host disk-dominated galaxies, featuring specific angular momentum in the stars close to that in the overall halo (see Romanowsky & Fall 2012; Shi et al. 2017; Lapi et al. 2018); the resulting long gas infall timescales and quiet star formation histories yield a much less dramatic size and kinematic evolution for disk-dominated galaxies. We note that in some instances, late-time gas recollapse/regrowth around preformed bulges can also contribute to build up disks and to explain the diversity in the bulge-to-disk ratios observed locally (e.g., Bernardi et al. 2014; Moffett et al. 2016).

In a future perspective, the outcomes of our study can provide inspiration toward solving the following hot issues.

1. Improving the (sub-grid) physical recipes implemented in theoretical models and simulations. In particular, the puffing-up that follows a substantial gas removal from the inner regions by stellar and/or BH feedback has not yet been included or at least not been properly treated in cosmological simulations. In the past years, this process has been overlooked by the community, since the short timescale for equilibrium recovery after the puffing versus the relatively young ages of $z \sim 2$ quiescent galaxies was an argument made against it. The most recent data indicate that although compact with respect to local ETGs, $z \sim 2$ quiescent galaxies feature sizes significantly larger than compact star-forming objects at similar redshift, which indicates that puffing-up has already affected them. Moreover, we have stressed the essential role of the puffing-up process in reducing the large dispersion expected and observed in the size of compact star-forming systems. Including the puffing-up process in numerical simulations could strongly alleviate problems in reproducing the size distributions of local ETGs and of their progenitors, without adopting extreme feedback or dry mergers prescriptions.

2. Tuning aimed at numerical experiments focused on specific processes. Specifically, it would be extremely interesting to elucidate in detail (i) the role of the biased collapse in setting a low initial specific angular momentum for the gas located in the halo inner regions; (ii) the effectiveness of the compaction via clump/gas migration and outward redistribution of angular momentum versus feedback processes; (iii) the development of violent relaxation in the inner region to cause a transition from a fully rotation-dominated to a significantly dispersion-endowed configuration; and (iv) the possibility that the latter process could also trigger accretion onto the central supermassive BH. Current numerical simulations aimed at investigating clump and gas migration often set as initial conditions a rotationally

supported disk with typical size of several kpcs; this means that the initial angular momentum of gas and clumps is quite high, implying migration timescales of about a few 10^8 years. However, our analysis based on the biased collapse scenario envisages that most of the final stellar component is formed from gas initially characterized by a rather low specific angular momentum; such gas is not rotationally supported on the fragmentation scale around several kpc, and can infall down to appreciably smaller radii on the order of kpc, maintaining its original angular momentum. The infall halts at the centrifugal barrier, where migration in the innermost regions can occur via dynamical friction over much shorter migration timescales of about 10^6 years. A numerical test of this scenario requires honed simulations with apt initial conditions, and high space/time resolution.

3. Planning future multiband, high-resolution observations on high-redshift star-forming/ quiescent galaxies and quasars. For example, it would be very interesting to compare the sizes observed in the far-IR/submillimeter band with that inferred from radio data to shed light on the spatial scales where radio emission originates in dusty star-forming galaxies; this will likely become achievable with SKA and its precursors. Other important observations concern kinematic measurements in ETG progenitors, which would constitute crucial tests of our scenario. In high-z star-forming galaxies we predict a high $v/\sigma \lesssim 10$ ratio of the gas component in the inner dust-obscured, star-forming regions, in rapid transition toward lower values $\lesssim 2$ via violent relaxation processes; the task is challenging but may be feasible with high-resolution measurements of CO (or other) line profiles by ALMA, especially on gravitationally lensed objects. On the other hand, in high-z quiescent galaxies, we expect a stellar velocity ratio $(v/\sigma)_\star \gtrsim 0.5$; there the measurements at $z \gtrsim 1$ are currently scarce, but their number is expected to increase appreciably in the era of the *James Webb Space Telescope* (*JWST*). Finally, other interesting observations concern extremely high-redshift quasars; a relevant example is the object J1342 + 0928 at $z \sim 7.5$ studied with JVLA (see Venemans et al. 2017a; Bañados et al. 2018). Following Equation (7), we expect an infall of about $10^{11}\,M_\odot$ in gas mass (corresponding to the inferred stellar mass of the host, see Venemans et al. 2017a) to occur over a timescale of about 10^8 years, significantly shorter than the Hubble time $\lesssim 700\,$Myr at the observed redshift. In addition, based on Equation (17), we expect a quite small size $\lesssim 0.5\,$kpc for the stellar and dust distributions. These specific predictions might be tested by ALMA observations at a resolution of ~ 0.1 arcsec.

In summary, we have highlighted the physical mechanisms that in ETG progenitors are responsible for the moderate SFRs $\lesssim 50$–$200\,M_\odot\,\mathrm{yr}^{-1}$ probed by UV data on scales of several kpcs, for the much higher SFRs $\lesssim 500$–$2000\,M_\odot\,\mathrm{yr}^{-1}$ probed by far-IR data on (sub-)kpc size, and for the resulting stellar mass growth $M_\star \sim 10^{11}\,M_\odot$ over timescales of some 10^8 years on spatial scales of a few to several kpcs, as probed by near-IR observations of quiescent galaxies. The corresponding number densities of UV-selected versus far-IR selected star-forming galaxies versus quiescent galaxies have been quantitatively computed via the continuity equation and positively compared with the observed statistics by Lapi

et al. ([2017a](#)). The dramatic increase in size from compact star-forming toward quiescent galaxies at similar redshift is an additional manifestation of the BH-galaxy coevolution, adding to the α-enhancement and to the massive outflows detected in quasar hosts at high redshift. To follow the driving processes via numerical simulations, time and spatial resolution should be privileged over large volumes because of the quite short time- and lengthscales involved. In fact, many observational and theoretical aspects of our analysis suggest a biased collapse scenario for ETG formation, envisaging that the low specific angular momentum of local massive ellipticals has essentially been imprinted since the very beginning, and that in situ processes are more relevant than mergers in driving most of their stellar and BH mass growth.

Appendix A
Mass Contrasts

In this appendix we provide explicit computation of the mass contrasts at the relevant size scales used in the main text. The critical radius R_Q for clump fragmentation is given by the equation

$$R_Q = \frac{j_{\text{inf}}\, Q}{\sqrt{2}\, \sigma}\, \delta_{\text{gas}}(R_Q), \qquad (32)$$

where the gas mass contrast is defined as $\delta_{\text{gas}}(R_Q) \equiv M_{\text{gas}}(<R_Q)/M_{\text{tot}}(<R_Q)$.

We assume that the baryonic mass within R_Q is constituted by all the infalling mass $M_{\text{inf}} = f_{\text{inf}} f_b M_H$, and that the gas mass can be estimated as $M_{\text{gas}} \simeq M_{\text{inf}} - M_\star$; this implies that the gas fraction reads $f_{\text{gas}} \equiv M_{\text{gas}}/M_{\text{inf}} \approx 1 - f_\star/f_{\text{inf}}$, with typical values of about $\gtrsim 0.5$, as observed in high-redshift disks (see Saintonge et al. [2013](#); Tacconi et al. [2013](#), [2018](#); Genzel et al. [2015](#); Barro et al. [2017](#)). Most of this gas mass is then evacuated from the galaxy after one Gyr by feedback from the central supermassive BH/quasar (see Section [3.3](#)). The DM mass can be written as $M_H(<R_Q) = 0.1\, M_H\, (R_Q/0.1\, R_H)^2$, since $M_H(<R) \propto R$ for $R \gtrsim 0.1\, R_H$ and $M_H(<R) \propto R^2$ for $R \lesssim 0.1\, R_H$ approximately hold; a posteriori, one can verify that R_Q falls in the latter radial range. All in all, the gas mass contrast is given by

$$\delta_{\text{gas}}(R_Q) \simeq \frac{f_{\text{gas}}\, f_{\text{inf}}\, f_b\, M_H}{f_{\text{inf}}\, f_b\, M_H + 0.1\, M_H\, (R_Q/0.1\, R_H)^2}$$
$$= \frac{f_{\text{gas}}}{1 + x_Q^2/0.1\, f_{\text{inf}}\, f_b}, \qquad (33)$$

where $x_Q \equiv R_Q/R_H$. Thus using Equation ([32](#)) yields the implicit equation

$$x_Q \approx \frac{j_{\text{inf}}\, Q}{\sqrt{2}\, \sigma\, R_H}\, \frac{f_{\text{gas}}}{1 + x_Q^2/0.1\, f_{\text{inf}}\, f_b}. \qquad (34)$$

Using the reference values $j_{\text{inf}} \approx 1.4 \times 10^3\,\text{km s}^{-1}$ kpc, $f_{\text{inf}} \approx 0.6$, $f_\star \approx 0.2$, $Q \approx 1$, and $\sigma \approx 60\,\text{km s}^{-1}$ applying for $M_\star \approx 10^{11}\, M_\odot$, the numerical solution yields $x_Q \approx 0.05$, corresponding to $\delta_{\text{gas}}(R_Q) \approx 0.5$. We stress that to obtain the quantitative results on R_Q presented in the figures of the main text, this computation of $\delta_{\text{gas}}(R_Q)$ has been performed with the detailed dependence of the parameters on stellar mass.

So far, we have neglected the adiabatic contraction of the DM component; we now take it into account with an iterative scheme. The classic equation to describe the process is

$$r_f\, [M_D(<r_f) + M_i(<r_i)(1 - m_D)] = r_i\, M_i(<r_i). \qquad (35)$$

where r_i and r_f are the radii before and after contraction, $M_D(<r_i)$ is the mass in the disk within r_i, m_D is the fraction of mass in the disk, and $M_i(<r_i)$ is the DM mass within r_i. In the present context, we can identify $r_f \to R_Q$, where R_Q is the known solution without adiabatic contraction, $r_i \to \tilde{R}_Q$ where $\tilde{R}_Q$ is the unknown starting radius with adiabatic contraction, $M_D(<r_f) \equiv M_\star = f_\star f_b M_H$, $m_D \equiv f_\star f_b$, and $M_i(<r_i) \equiv 0.1\, M_H\, (\tilde{R}_Q/0.1\, R_H)^2$. Then Equation ([35](#)) becomes

$$R_Q\left[M_\star + (1 - f_\star f_b)0.1\, M_H\left(\frac{\tilde{R}_Q}{0.1\, R_H}\right)^2 \right]$$
$$= \tilde{R}_Q\, 0.1\, M_H\left(\frac{\tilde{R}_Q}{0.1\, R_H}\right)^2, \qquad (36)$$

and defining $\tilde{x}_Q \equiv \tilde{R}_Q/R_H$ leads to the algebraic equation

$$x_Q\, [0.1 f_\star f_b + (1 - f_\star f_b)\tilde{x}_Q^2] = \tilde{x}_Q^3. \qquad (37)$$

Using the solution $x_Q \approx 0.05$ from Equation ([34](#)) yields $\tilde{x}_Q \approx 0.08$, corresponding to $\delta_{\text{gas}}(R_Q) \approx 0.38$. In addition, the baryonic contrast $\delta(R_Q) \equiv M_{\text{inf}}/M_{\text{tot}}(<R_Q)$ involving all the infalling mass is given by

$$\delta(R_Q) \simeq \frac{f_{\text{inf}}\, f_b\, M_H}{f_{\text{inf}}\, f_b\, M_H + 0.1\, M_H\, (R_Q/0.1\, R_H)^2}$$
$$= \frac{1}{1 + x_Q^2/0.1\, f_{\text{inf}}\, f_b}, \qquad (38)$$

and takes on values of about $\delta(R_Q) \approx 0.6$.

The same line of reasoning can be applied to computing the radius R_{rot} of the centrifugal barrier, given by

$$R_{\text{rot}} = \frac{j_{\text{inf}}^2}{G\, M_{\text{inf}}}\, \delta(R_{\text{rot}}), \qquad (39)$$

where the baryonic mass contrast is now defined as $\delta(R_{\text{rot}}) \equiv M_{\text{inf}}/M_{\text{tot}}(<R_{\text{rot}})$. We derive

$$\delta(R_{\text{rot}}) \approx \frac{1}{1 + x_{\text{rot}}^2/0.1\, f_{\text{inf}}\, f_b}, \qquad (40)$$

where $x_{\mathrm{rot}} \equiv R_{\mathrm{rot}}/R_{\mathrm{H}}$ is given by the implicit equation

$$x_{\mathrm{rot}} \approx \frac{j_{\mathrm{inf}}^2}{G\,M_{\mathrm{inf}}\,R_{\mathrm{H}}} \frac{1}{1 + x_{\mathrm{rot}}^2/0.1\,f_{\mathrm{inf}}\,f_b}. \quad (41)$$

The numerical solution yields $x_{\mathrm{rot}} \approx 0.0099$, corresponding to $\delta(R_{\mathrm{rot}}) \approx 0.99$.

We now introduce the effects of adiabatic contraction, and the corrected radius $\tilde{R}_{\mathrm{rot}} \equiv \tilde{x}_{\mathrm{rot}} R_{\mathrm{H}}$ is determined by

$$x_{\mathrm{rot}}\,[0.1\,f_\star\,f_b + (1 - f_\star\,f_b)\tilde{x}_{\mathrm{rot}}^2] = \tilde{x}_{\mathrm{rot}}^3, \quad (42)$$

which yields $\tilde{x}_{\mathrm{rot}} \approx 0.036$, corresponding to $\delta(R_{\mathrm{rot}}) \approx 0.88$. In addition, the gas mass contrast $\delta_{\mathrm{gas}}(R_{\mathrm{rot}}) \equiv M_{\mathrm{gas}}/M_{\mathrm{tot}}(<R_{\mathrm{rot}})$ is given by

$$\delta_{\mathrm{gas}}(R_{\mathrm{rot}}) \simeq \frac{f_{\mathrm{gas}}\,f_{\mathrm{inf}}\,f_b\,M_{\mathrm{H}}}{f_{\mathrm{inf}}\,f_b\,M_{\mathrm{H}} + 0.1\,M_{\mathrm{H}}\,(R_{\mathrm{rot}}/0.1\,R_{\mathrm{H}})^2}$$
$$= \frac{f_{\mathrm{gas}}}{1 + x_{\mathrm{rot}}^2/0.1\,f_{\mathrm{inf}}\,f_b}, \quad (43)$$

and takes on values of about $\delta_{\mathrm{gas}}(R_{\mathrm{rot}}) \approx 0.57$.

Finally, we aim at computing the radius R_b where the baryonic mass dominates the gravitational potential over the DM. To first approximation, this is given by

$$\frac{G\,M_{\mathrm{inf}}}{R_b} \approx \frac{G\,M_{\mathrm{H}}(<R_b)}{R_b}, \quad (44)$$

corresponding to a baryonic mass contrast $\delta(R_b) \equiv M_{\mathrm{inf}}/M_{\mathrm{tot}}(<R_b) \approx 0.5$. Neglecting adiabatic contraction and assuming the scaling $M_{\mathrm{H}}(<R_b) \simeq M_{\mathrm{H}}\,x_b^2/0.1$ with $x_b \equiv R_b/R_{\mathrm{H}}$ yields $x_b \simeq \sqrt{0.1\,f_{\mathrm{inf}}\,f_b} \approx 0.098$.

We now introduce the effects of adiabatic contraction, and the corrected radius $\tilde{R}_b \equiv \tilde{x}_b R_{\mathrm{H}}$ is determined by

$$x_b\,[0.1\,f_\star\,f_b + (1 - f_\star\,f_b)\tilde{x}_b^2] = \tilde{x}_b^3, \quad (45)$$

which yields $\tilde{x}_b \approx 0.12$, corresponding to a mass contrast $\delta(R_b) \approx 0.41$. All in all, the radius R_b writes

$$R_b \approx \sqrt{[\delta(R_b)^{-1} - 1]\,0.1\,f_{\mathrm{inf}}\,f_b}\;R_{\mathrm{H}}. \quad (46)$$

ORCID iDs

A. Lapi ⬤ https://orcid.org/0000-0002-4882-1735
F. Shankar ⬤ https://orcid.org/0000-0001-8973-5051
A. Bressan ⬤ https://orcid.org/0000-0002-7922-8440

References

Alexander, D. M., & Hickox, R. C. 2012, NewAR, 56, 93
Almaini, O., wild, V., Maltby, D.T., et al. 2017, MNRAS, 472, 1401
Andrews, B. H., & Thompson, T. A. 2011, ApJ, 727, 97
Annibali, F., Bressan, A., Rampazzo, R., Zeilinger, W. W., & Danese, L. 2007, A&A, 463, 455
Aravena, M., Spilker, J. S., Bethermin, M., et al. 2016, MNRAS, 457, 4406
Aversa, R., Lapi, A., De Zotti, G., Shankar, F., & Danese, L. 2015, ApJ, 810, 74
Bañados, E., Venemans, B. P., Mazzucchelli, C., et al. 2018, Natur, 553, 473
Barnes, J., & Efstathiou, G. 1987, ApJ, 319, 575
Barro, G., Faber, S. M., Dekel, A., et al. 2016a, ApJ, 820, 120
Barro, G., Kriek, M., Pérez-González, P. G., et al. 2016b, ApJL, 827, L32
Barro, G., Kriek, M., Perez-Gonzalez, P. G., et al. 2017, ApJL, 851, L40
Barro, G., Trump, J. R., Koo, D. C., et al. 2014, ApJ, 795, 145
Baumgardt, H., & Kroupa, P. 2007, MNRAS, 380, 1589
Beckmann, R. S., Devriendt, J., Slyz, A., et al. 2017, MNRAS, 472, 949
Behroozi, P. S., Wechsler, R. H., & Conroy, C. 2013, ApJ, 770, 57
Belli, S., Newman, A. B., & Ellis, R. S. 2017, ApJ, 834, 18
Belli, S., Newman, A. B., Ellis, R. S., & Konidaris, N. P. 2014, ApJL, 788, L29
Bernardi, M., Meert, A., Vikram, V., et al. 2014, MNRAS, 443, 874
Béthermin, M., Daddi, E., Magdis, G., et al. 2015, A&A, 573, A113
Biermann, P., & Shapiro, S. L. 1979, ApJL, 230, L33
Binney, J. 2005, MNRAS, 363, 937
Birnboim, Y., & Dekel, A. 2003, MNRAS, 345, 349
Boily, C. M., & Kroupa, P. 2003, MNRAS, 338, 673
Bournaud, F. 2016, Galactic Bulges (Switzerland: Springer International Publishing), 355
Bournaud, F., Chapon, D., Teyssier, R., et al. 2011, ApJ, 730, 4
Bournaud, F., Perret, V., Renaud, F., et al. 2014, ApJ, 780, 57
Bourne, N., Dunlop, J. S., Merlin, E., et al. 2017, MNRAS, 467, 1360
Bouwens, R. J., Aravena, M., De Carli, R., et al. 2016, ApJ, 833, 72
Bouwens, R. J., Oesch, P. A., Illingworth, G. D., Ellis, R. S., & Stefanon, M. 2017, ApJ, 843, 129
Boylan-Kolchin, M., Ma, C.-P., & Quataert, E. 2008, MNRAS, 383, 93
Braun, H., & Schmidt, W. 2012, MNRAS, 421, 1838
Buitrago, F., Trujillo, I., Curtis-Lake, E., et al. 2017, MNRAS, 466, 4888
Bullock, J. S., Dekel, A., Kolatt, T. S., et al. 2001, ApJ, 555, 240
Burkert, A., Forster Schreiber, N. M., Genzel, R., et al. 2016, ApJ, 826, 214
Cappellari, M. 2016, ARA&A, 54, 597
Cappellari, M., McDermid, R. M., Alatalo, K., et al. 2013, MNRAS, 432, 1862
Caputi, K. I., Ilbert, O., Laigle, C., et al. 2015, ApJ, 810, 73
Carniani, S., Marconi, A., Maiolino, R., et al. 2017, A&A, 605, A105
Ceverino, D., Dekel, A., & Bournaud, F. 2010, MNRAS, 404, 2151
Chabrier, G. 2003, ApJL, 586, L133
Chartas, G., Saez, C., Brandt, W. N., Giustini, M., & Garmire, G. P. 2009, ApJ, 706, 644
Choi, J., Conroy, C., Moustakas, J., et al. 2014, ApJ, 792, 95
Cimatti, A., Cassata, P., Pozzetti, L., et al. 2008, A&A, 482, 21
Cimatti, A., Daddi, E., Renzini, A., et al. 2004, Natur, 430, 184
Ciotti, L., & Ostriker, J. P. 2007, ApJ, 665, 1038
Citro, A., Pozzetti, L., Moresco, M., & Cimatti, A. 2016, A&A, 592, A19
Cole, S., Lacey, C. G., Baugh, C. M., & Frenk, C. S. 2000, MNRAS, 319, 168
Cooray, A., Calanog, J., Wardlow, J. L., et al. 2014, ApJ, 790, 40
Daddi, E., Renzini, A., Pirzkal, N., et al. 2005, ApJ, 626, 680
Damjanov, I., McCarthy, P. J., Abraham, R. G., et al. 2009, ApJ, 695, 101
Danovich, M., Dekel, A., Hahn, O., Ceverino, D., & Primack, J. 2015, MNRAS, 449, 2087
D'Onghia, E., & Burkert, A. 2004, ApJL, 612, L13
Davidzon, I., Ilbert, O., Laigle, C., et al. 2017, A&A, 605, A70
Decarli, R., Walter, F., Aravena, M., et al. 2016, ApJ, 833, 70
Decarli, R., Walter, F., Venemans, B. P., et al. 2017, Natur, 545, 457
DeGraf, C., Dekel, A., Gabor, J., & Bournaud, F. 2017, MNRAS, 466, 1462
Dekel, A., & Birnboim, Y. 2008, MNRAS, 383, 119
Dekel, A., Birnboim, Y., Engel, G., et al. 2009, Natur, 457, 451
Dekel, A., & Burkert, A. 2014, MNRAS, 438, 1870
Dekel, A., & Krumholz, M. R. 2013, MNRAS, 432, 455
Delvecchio, I., Lutz, D., Berta, S., et al. 2015, MNRAS, 449, 373
Di Teodoro, E. M., Fraternali, F., & Miller, S. H. 2016, A&A, 594, A77
Duncan, K., Conselice, C. J., Mortlock, A., et al. 2014, MNRAS, 444, 2960
Dunlop, J. S., McLure, R. J., Biggs, A. D., et al. 2017, MNRAS, 466, 861
Dutton, A. A., Conroy, C., van den Bosch, F. C., et al. 2011, MNRAS, 416, 322
Eke, V., Efstathiou, G., & Wright, L. 2000, MNRAS, 315, L18
Elmegreen, D. M., Elmegreen, B. G., & Ferguson, T. E. 2005, ApJL, 623, L71
Elmegreen, D. M., Elmegreen, B. G., Ravindranath, S., & Coe, D. A. 2007, ApJ, 658, 763
Emsellem, E., Cappellari, M., Krajnovic, D., et al. 2007, MNRAS, 379, 401
Faber, S. M., & Jackson, R. E. 1976, ApJ, 204, 668
Fall, S. M. 2002, in ASP Conf. Ser. 275, Disks of Galaxies: Kinematics, Dynamics and Peturbations, ed. E. Athanassoula, A. Bosma, & R. Mujica (San Francisco, CA: ASP), 389
Fan, L., Lapi, A., Bressan, A., et al. 2010, ApJ, 718, 1460
Fan, L., Lapi, A., De Zotti, G., & Danese, L. 2008, ApJL, 689, L101
Feldmann, R. 2015, MNRAS, 449, 3274
Finlator, K., Oh, S. P., Ozel, F., & Davé, R. 2012, MNRAS, 427, 2464
Fiore, F., Feruglio, C., Shankar, F., et al. 2017, A&A, 601, A143
Furlong, M., Bower, R. G., Crain, R. A., et al. 2017, MNRAS, 465, 722
Gabor, J. M., & Bournaud, F. 2013, MNRAS, 434, 606
Gallazzi, A., Bell, E. F., Zibetti, S., Brinchmann, J., & Kelson, D. D. 2014, ApJ, 788, 72

Gallazzi, A., Charlot, S., Brinchmann, J., & White, S. D. M. 2006, MNRAS, 370, 1106
Genel, S., Nelson, D., Pillepich, A., et al. 2018, MNRAS, 474, 3976
Genzel, R., Forster Schreiber, N. M., Lang, P., et al. 2014, ApJ, 785, 75
Genzel, R., Forster Schreiber, N. M., Ubler, H., et al. 2017, Natur, 543, 397
Genzel, R., Newman, S., Jones, T., et al. 2011, ApJ, 733, 101
Genzel, R., Tacconi, L. J., Lutz, D., et al. 2015, ApJ, 800, 20
Geyer, M. P., & Burkert, A. 2001, MNRAS, 323, 988
Glazebrook, K., Schreiber, C., Labbé, I., et al. 2017, Natur, 544, 71
Goldreich, P., & Tremaine, S. 1980, ApJ, 241, 425
Gomez-Guijarro, C., Toft, S., Karim, A., et al. 2018, ApJ, in press (arXiv:1802.07751)
Gonzalez, A. H., Sivanandam, S., Zabludoff, A. I., & Zaritsky, D. 2013, ApJ, 778, 14
Goodwin, S. P., & Bastian, N. 2006, MNRAS, 373, 752
Granato, G. L., De Zotti, G., Silva, L., Bressan, A., & Danese, L. 2004, ApJ, 600, 580
Grazian, A., Fontana, A., Santini, P., et al. 2015, A&A, 575, A96
Gruppioni, C., Calura, F., Pozzi, F., et al. 2015, MNRAS, 451, 3419
Gruppioni, C., Pozzi, F., Rodighiero, G., et al. 2013, MNRAS, 432, 23
Guo, Y., Rafelski, M., Bell, E. F., et al. 2018, ApJ, 853, 108
Hill, R., Chapman, S. C., Scott, D., et al. 2017, MNRAS, in press (arXiv:1710.02231)
Hills, J. G. 1980, ApJ, 235, 986
Hodge, J. A., Karim, A., Smail, I., et al. 2013, ApJ, 768, 91
Hodge, J. A., Swinbank, A. M., Simpson, J. M., et al. 2016, ApJ, 833, 103
Hopkins, P. F., Hernquist, L., Cox, T. J., Robertson, B., & Springel, V. 2006, ApJS, 163, 50
Hopkins, P. F., Quataert, E., & Murray, N. 2012, MNRAS, 421, 3522
Hudson, M. J., Gillis, B. R., Coupon, J., et al. 2015, MNRAS, 447, 298
Huertas-Company, M., Perez-Gonzalez, P. G., Mei, S., et al. 2015, ApJ, 809, 95
Huynh, M. T., Emonts, B. H. C., Kimball, A. E., et al. 2017, MNRAS, 467, 1222
Hyde, J. B., & Bernardi, M. 2009, MNRAS, 394, 1978
Ikarashi, S., Ivison, R. J., Caputi, K. I., et al. 2015, ApJ, 810, 133
Ikarashi, S., Ivison, R. J., Caputi, K. I., et al. 2017, ApJ, 835, 286
Ilbert, O., McCracken, H. J., le Fevre, O., et al. 2013, A&A, 556, A55
Iliev, I. T., Mellema, G., Shapiro, P. R., & Pen, U.-L. 2007, MNRAS, 376, 534
Immeli, A., Samland, M., Westera, P., & Gerhard, O. 2004, ApJ, 611, 20
Jimenez-Andrade, E. F., Magnelli, B., Karim, A., et al. 2018, A&A, in press (arXiv:1710.10181)
Johnson, H. L., Harrison, C. M., Swinbank, A. M., et al. 2018, MNRAS, 474, 5076
Johnson, J. L., Whalen, D. J., Li, H., & Holz, D. E. 2013, ApJ, 771, 116
Karim, A., Swinbank, A. M., Hodge, J. A., et al. 2013, MNRAS, 432, 2
Khochfar, S., & Ostriker, J. P. 2008, ApJ, 680, 54
Khochfar, S., & Silk, J. 2006, ApJL, 648, L21
Koprowski, M., Dunlop, J. S., Michalowski, M. J., et al. 2016, MNRAS, 458, 4321
Koprowski, M. P., Dunlop, J. S., Michalowski, M. J., Cirasuolo, M., & Bowler, R. A. A. 2014, MNRAS, 444, 117
Kormendy, J., & Ho, L. C. 2013, ARA&A, 51, 511
Kravtsov, A., Vikhlinin, A., & Meshscheryakov, A. 2014, (arXiv:1401.7329)
Kriek, M., Conroy, C., van Dokkum, P. G., et al. 2016, Natur, 540, 248
Krumholz, M. R., & Dekel, A. 2012, ApJ, 753, 16
Krumholz, M. R., Dekel, A., & McKee, C. F. 2012, ApJ, 745, 69
Kurczynski, P., Gawiser, E., Acquaviva, V., et al. 2016, ApJL, 820, L1
Lagos, C. d. P., Theuns, T., Stevens, A. R. H., et al. 2017, MNRAS, 464, 3850
Lang, P., Forster Schreiber, N. M., & Genzel, R. 2017, ApJ, 840, 92
Lange, R., Driver, S. P., & Robotham, A. S. G. 2015, MNRAS, 447, 2603
Lapi, A., Gonzalez-Nuevo, J., Fan, L., et al. 2011, ApJ, 742, 24
Lapi, A., Mancuso, C., Bressan, A., & Danese, L. 2017a, ApJ, 847, 13
Lapi, A., Mancuso, C., Celotti, A., & Danese, L. 2017b, ApJ, 835, 37
Lapi, A., Raimundo, S., Aversa, R., et al. 2014, ApJ, 782, 69
Lapi, A., Salucci, P., & Danese, L. 2018, ApJ, submitted
Lapi, A., Shankar, F., Mao, J., et al. 2006, ApJ, 650, 42
Law, D. R., Steidel, C. C., Erb, D. K., et al. 2009, ApJ, 697, 2057
Lilly, S. J., Carollo, C. M., Pipino, A., et al. 2013, ApJ, 772, 119
Lonoce, I., Longhetti, M., Maraston, C., et al. 2015, MNRAS, 454, 3912
Macció, A. V., Dutton, A. A., van den Bosch, F. C., et al. 2007, MNRAS, 378, 55
Maller, A. H., Dekel, A., & Somerville, R. 2002, MNRAS, 329, 423
Man, A. W. S., Greve, T. R., Toft, S., et al. 2016, ApJ, 820, 11
Mancuso, C., Lapi, A., Shi, J., et al. 2016a, ApJ, 823, 128
Mancuso, C., Lapi, A., Shi, J., et al. 2016b, ApJ, 833, 152

Mandelbaum, R., Wang, W., Zu, Y., et al. 2016, MNRAS, 457, 3200
Mandelker, N., Dekel, A., Ceverino, D., et al. 2014, MNRAS, 443, 3675
Mandelker, N., Dekel, A., Ceverino, D., et al. 2017, MNRAS, 464, 635
Martin-Navarro, I., Vazdekis, A., Falcon-Barroso, J., et al. 2018, MNRAS, 475, 3700
Massardi, M., Enia, A. F. M., Negrello, M., et al. 2018, A&A, 610, A53
Mihos, J. C., & Hernquist, L. 1996, ApJ, 464, 641
Mo, H., van den Bosch, F. C., & White, S. 2010, Galaxy Formation and Evolution (Cambridge: Cambridge Univ. Press)
Mo, H. J., Mao, S., & White, S. D. M. 1998, MNRAS, 295, 319
Moffett, A. J., Lange, R., Driver, S. P., et al. 2016, MNRAS, 462, 4336
More, S., van den Bosch, F. C., Cacciato, M., et al. 2011, MNRAS, 410, 210
Moster, B. P., Naab, T., & White, S. D. M. 2013, MNRAS, 428, 3121
Moster, B. P., Naab, T., & White, S. D. M. 2017, MNRAS, in press (arXiv:1705.05373)
Mullaney, J. R., Daddi, E., Bethermin, M., et al. 2012, ApJL, 753, L30
Murray, N., Quataert, E., & Thompson, T. A. 2005, ApJ, 618, 569
Murray, N., Quataert, E., & Thompson, T. A. 2010, ApJ, 709, 191
Naab, T., Johansson, P. H., & Ostriker, J. P. 2009, ApJL, 699, L178
Narayanan, D., Turk, M., Feldmann, R., et al. 2015, Natur, 525, 496
Navarro, J. F., Frenk, C. S., & White, S. D. M. 1997, ApJ, 490, 493
Nayyeri, H., Keele, M., Cooray, A., et al. 2016, ApJ, 823, 17
Negrello, M., Amber, S., Amvrosiadis, A., et al. 2017, MNRAS, 465, 3558
Negrello, M., Hopwood, R., Dye, S., et al. 2014, MNRAS, 440, 1999
Newman, A. B., Belli, S., & Ellis, R. S. 2015, ApJL, 813, L7
Noguchi, M. 1999, ApJ, 514, 77
Nomoto, K., Kobayashi, C., & Tominaga, N. 2013, ARA&A, 51, 457
Novak, M., Smolcic, V., Delhaize, J., et al. 2017, A&A, 602, A5
Oklopcic, A., Hopkins, P. F., Feldmann, R., et al. 2017, MNRAS, 465, 952
Page, M. J., Symeonidis, M., Vieira, J., et al. 2012, Natur, 485, 213
Pawlik, A. H., Schaye, J., & van Scherpenzeel, E. 2009, MNRAS, 394, 1812
Planck Collaboration XIII 2016, A&A, 594, A13
Pope, A., Montana, A., Battisti, A., et al. 2017, ApJ, 838, 137
Prochaska, J. X., & Hennawi, J. F. 2009, ApJ, 690, 1558
Ragone-Figueroa, C., & Granato, G. L. 2011, MNRAS, 414, 3690
Renzini, A. 2006, ARA&A, 44, 141
Richstone, D. O., & Potter, M. D. 1982, ApJ, 254, 451
Riechers, D. A., Daisy Leung, T. K., Ivison, R., et al. 2017, ApJ, 850, 1
Rodighiero, G., Brusa, M., Daddi, E., et al. 2015, ApJL, 800, L10
Rodighiero, G., Daddi, E., Baronchelli, I., et al. 2011, ApJL, 739, L40
Rodriguez-Gomez, V., Genel, S., Vogelsberger, M., et al. 2015, MNRAS, 449, 49
Rodriguez-Gomez, V., Pillepich, A., Sales, L. V., et al. 2016, MNRAS, 458, 2371
Rodriguez-Puebla, A., Avila-Reese, V., Yang, X., et al. 2015, ApJ, 799, 130
Romano, D., Karakas, A. I., Tosi, M., & Matteucci, F. 2010, A&A, 522, A32
Romanowsky, A. J., & Fall, S. M. 2012, ApJS, 203, 17
Rowan-Robinson, M., Oliver, S., Wang, L., et al. 2016, MNRAS, 461, 1100
Rujopakarn, W., Nyland, K., Rieke, G. H., et al. 2018, ApJL, 854, L4
Saintonge, A., Lutz, D., Genzel, R., et al. 2013, ApJ, 778, 2
Salmon, B., Papovich, C., Finkelstein, S. L., et al. 2015, ApJ, 799, 183
Santini, P., Fontana, A., Castellano, M., et al. 2017, ApJ, 847, 76
Schreiber, C., Labbé, I., Glazebrook, K., et al. 2018, A&A, 611, A22
Schreiber, C., Pannella, M., Leiton, R., et al. 2017, A&A, 599, A134
Scoville, N., Aussel, H., Sheth, K., et al. 2014, ApJ, 783, 84
Scoville, N., Lee, N., Vanden Bout, P., et al. 2017, ApJ, 837, 150
Scoville, N., Sheth, K., Aussel, H., et al. 2016, ApJ, 820, 83
Shankar, F., Bernardi, M., & Haiman, Z. 2009, ApJ, 694, 867
Shankar, F., Bernardi, M., Sheth, R. K., et al. 2016, MNRAS, 460, 3119
Shankar, F., Lapi, A., Salucci, P., de Zotti, G., & Danese, L. 2006, ApJ, 643, 14
Shankar, F., Marulli, F., Bernardi, M., et al. 2013, MNRAS, 428, 109
Shankar, F., Mei, S., Huertas-Company, M., et al. 2014, MNRAS, 439, 3189
Shen, S., Mo, H. J., White, S. D. M., et al. 2003, MNRAS, 343, 978
Shi, J., Lapi, A., Mancuso, C., Wang, H., & Danese, L. 2017, ApJ, 843, 105
Shibuya, T., Ouchi, M., & Harikane, Y. 2015, ApJS, 219, 15
Shlosman, I., & Noguchi, M. 1993, ApJ, 414, 474
Shull, J. M., Harness, A., Trenti, M., & Smith, B. D. 2012, ApJ, 747, 100
Silk, J., & Rees, M. J. 1998, A&A, 331, L1
Simpson, J. M., Smail, I., Swinbank, A. M., et al. 2015, ApJ, 807, 128
Simpson, J. M., Smail, I., Wang, W.-H., et al. 2017, ApJL, 844, L10
Siudek, M., Małek, K., Scodeggio, M., et al. 2017, A&A, 597, A107
Song, M., Finkelstein, S. L., Ashby, M. L. N., et al. 2016, ApJ, 825, 5
Speagle, J. S., Steinhardt, C. L., Capak, P. L., & Silverman, J. 2014, ApJS, 214, 15
Spilker, J. S., Marrone, D. P., Aravena, M., et al. 2016, ApJ, 826, 112

Stanley, F., Alexander, D. M., Harrison, C. M., et al. 2017, MNRAS, 472, 2221
Stanley, F., Harrison, C. M., Alexander, D. M., et al. 2015, MNRAS, 453, 591
Straatman, C. M. S., Labbé, I., & Spitler, L. R. 2015, ApJL, 808, L29
Strandet, M. L., Weiss, A., De Breuck, C., et al. 2017, ApJL, 842, L15
Strandet, M. L., Weiss, A., Vieira, J. D., et al. 2016, ApJ, 822, 80
Sutherland, R. S., & Dopita, M. A. 1993, ApJS, 88, 253
Swinbank, A. M., Harrison, C. M., Trayford, J., et al. 2017, MNRAS, 467, 3140
Tacconi, L. J., Genzel, R., Saintonge, A., et al. 2018, ApJ, 853, 179
Tacconi, L. J., Neri, R., Genzel, R., et al. 2013, ApJ, 768, 74
Tadaki, K.-I., Genzel, R., Kodama, T., et al. 2017a, ApJ, 834, 135
Tadaki, K.-I., Kodama, T., Nelson, E. J., et al. 2017b, ApJL, 841, L25
Talia, M., Pozzi, F., Vallini, L., et al. 2018, MNRAS, in press (arXiv:1802.06083)
Tasca, L. A. M., Le Févre, O., Hathi, N. P., et al. 2015, A&A, 581, A54
Teklu, A. F., Remus, R.-S., Dolag, K., et al. 2018, ApJL, 854, L28
Thomas, D., Maraston, C., Bender, R., & Mendes de Oliveira, C. 2005, ApJ, 621, 673
Thompson, T. A., Quataert, E., & Murray, N. 2005, ApJ, 630, 167
Toft, S., Zabl, J., Richard, J., et al. 2017, Natur, 546, 510
Tomczak, A. R., Quadri, R. F., Tran, K. H., et al. 2016, ApJ, 817, 118
Tomczak, A. R., Quadri, R. F., Tran, K.-V. H., et al. 2014, ApJ, 783, 85
Toomre, A. 1964, ApJ, 139, 1217
Trujillo, I., Forster Schreiber, N. M., Rudnick, G., et al. 2006, ApJ, 650, 18
Turner, O. J., Cirasuolo, M., Harrison, C. M., et al. 2017, MNRAS, 471, 1280
van de Sande, J., Kriek, M., Franx, M., et al. 2013, ApJ, 771, 85

van den Bosch, R. C. E. 2016, ApJ, 831, 134
van der Wel, A., Franx, M., van Dokkum, P. G., et al. 2014, ApJ, 788, 28
van der Wel, A., & van der Marel, R. P. 2008, ApJ, 684, 260
van Dokkum, P. G., Bezanson, R., & van der Wel, A. 2014, ApJ, 791, 45
van Dokkum, P. G., Franx, M., Kriek, M., et al. 2008, ApJL, 677, L5
van Dokkum, P. G., Kriek, M., & Franx, M. 2009, Natur, 460, 717
van Dokkum, P. G., Nelson, E. J., Franx, M., et al. 2015, ApJ, 813, 23
Veale, M., Ma, C.-P., & Greene, J. E. 2017, MNRAS, 471, 1428
Velander, M., van Uitert, E., Hoekstra, H., et al. 2014, MNRAS, 437, 2111
Venemans, B. P., Walter, F., Decarli, R., et al. 2017a, ApJL, 851, L8
Venemans, B. P., Walter, F., Decarli, R., et al. 2017b, ApJ, 837, 146
Venemans, B. P., Walter, F., Zschaechner, L., et al. 2016, ApJ, 816, 37
Vincenzo, F., Matteucci, F., Belfiore, F., & Maiolino, R. 2016, MNRAS, 455, 4183
Weiss, A., De Breuck, C., Marrone, D. P., et al. 2013, ApJ, 767, 88
White, S. D. M., & Frenk, C. S. 1991, ApJ, 379, 52
Wisnioski, E., Forster Schreiber, N. M., Wuyts, S., et al. 2015, ApJ, 799, 209
Wojtak, R., & Mamon, G. A. 2013, MNRAS, 428, 2407
Yildirim, A., van den Bosch, R.C.E., van de Ven, G., et al. 2017, MNRAS, 468, 4216
Zavala, J., Frenk, C. S., Bower, R., et al. 2016, MNRAS, 460, 4466
Zavala, J. A., Montana, A., Hughes, D. H., et al. 2018, NatAs, 2, 56
Zhao, D. H., Mo, H. J., Jing, Y. P., & Börner, G. 2003, MNRAS, 339, 12
Zjupa, J., & Springel, V. 2017, MNRAS, 466, 1625
Zolotov, A., Dekel, A., Mandelker, N., & Tweed, D. 2015, MNRAS, 450, 2327